

A Recalibration of Strong Line Oxygen Abundance Diagnostics via the Direct Method and Implications for the High Redshift Universe

Jonathan S. Brown,^{1*} Paul Martini,^{1,2} and Brett H. Andrews³

¹*Department of Astronomy, The Ohio State University, 140 West 18th Avenue, Columbus, OH 43210, USA*

²*Center for Cosmology and Astro-Particle Physics, The Ohio State University, 191 West Woodruff Avenue, Columbus, OH 43210, USA*

³*PITT PACC, Department of Physics and Astronomy, University of Pittsburgh, 3941 O'Hara Street, Pittsburgh, PA 15260, USA*

Accepted XXX. Received YYY; in original form ZZZ

ABSTRACT

We use direct method oxygen abundances in combination with strong optical emission lines, stellar masses (M_*), and star formation rates (SFRs) to recalibrate the N2, O3N2, and N2O2 oxygen abundance diagnostics. We stack spectra of $\sim 200,000$ star-forming galaxies from the Sloan Digital Sky Survey in bins of M_* and SFR offset from the star forming main sequence ($\Delta \log(\text{SSFR})$) to measure the weak emission lines needed to apply the direct method. All three new calibrations are reliable to within ± 0.10 dex from $\log(M_*/M_\odot) \sim 7.5 - 10.5$ and up to at least $200 M_\odot \text{ yr}^{-1}$ in SFR. The N2O2 diagnostic is the least subject to systematic biases. We apply the diagnostics to galaxies in the local universe and investigate the $M_* - Z - \text{SFR}$ relation. The N2 and O3N2 diagnostics suggest the SFR dependence of the $M_* - Z - \text{SFR}$ relation varies with both M_* and $\Delta \log(\text{SSFR})$, whereas the N2O2 diagnostic suggests a nearly constant dependence on SFR. We apply our calibrations to a sample of high redshift galaxies from the literature, and find them to be metal poor relative to local galaxies with similar M_* and SFR. The calibrations do reproduce direct method abundances of the local analogs. We conclude that the $M_* - Z - \text{SFR}$ relation evolves with redshift.

Key words: galaxies: active – galaxies: abundances – galaxies: evolution – galaxies: ISM – ISM: abundances

1 INTRODUCTION

Galaxies are continually undergoing chemical enrichment. Gas is condensed into stars, processed into heavier elements, and returned to the interstellar medium. This gas, enriched by the products of stellar nucleosynthesis and/or supernova ejecta, is reincorporated into new generations of stars, where it is enriched once again. A galaxy may also accrete low metallicity gas from the intergalactic medium, which both dilutes the ISM and provides fuel for a new generation of stars to form. This interplay between star formation, chemical enrichment, and accretion of new material is a central component of galaxy evolution.

An episode of star formation increases a galaxy's stellar mass and enriches the ISM. A substantial body of work has shown that there are correlations between stellar mass (M_*), star formation rate (SFR), and gas phase oxygen abundance. The correlation between M_* and gas phase oxygen abundance is called the Mass-Metallicity Relation (MZR;

Lequeux et al. 1979; Tremonti et al. 2004). The MZR extends from low mass, extremely metal deficient galaxies like Leo P (Skillman et al. 2013) up to massive galaxies with 2–3 times the solar oxygen abundance (Tremonti et al. 2004; Moustakas et al. 2011).

The MZR often serves as a benchmark for models of galaxy evolution because the details of the MZR are direct probes of the underlying physics. For instance, Tremonti et al. (2004) describe how the shape of the MZR requires galactic winds to efficiently remove metals from low mass galaxies. Subsequent cosmological models (e.g. Davé et al. 2006; Oppenheimer & Davé 2006; Finlator & Davé 2008; Davé et al. 2011b,a) incorporated winds into their cosmological models in order to better understand the origin of the MZR. In the context of their momentum driven wind models, the mass loading parameter $\eta \equiv \dot{M}_{\text{outflow}}/\dot{M}_*$ is proportional to the inverse of the velocity dispersion of the halo, which scales with the halo mass to the one third power, $\eta \propto 1/\sigma_h \propto M_h^{-1/3}$ (Murray et al. 2005; Oppenheimer & Davé 2006). Once the star formation has reached an equilibrium with the inflowing and outflow-

*E-mail: brown@astronomy.ohio-state.edu

ing gas, the metallicity is $Z = y/(1 + \eta)$ where y is the effective yield. In the limit that $\eta \gg 1$, the slope of the MZR is ultimately related to how M_* scales with M_h , since $\log(Z) \propto -\log(\eta) \propto \frac{1}{3}\log(M_h)$.

There is good observational evidence for a second parameter that affects the relationship between M_* and Z such that galaxies with higher star formation rates have lower metallicities at fixed stellar mass (the M_* - Z -SFR relation; Ellison et al. 2008; Mannucci et al. 2010; Lara-López et al. 2010). This relation is also apparent in high signal-to-noise ratio stacked spectra of SDSS galaxies (Andrews & Martini 2013). However, it has intriguingly not been seen in the CALIFA sample of 150 nearby galaxies studied with integral field spectroscopy by Sánchez et al. (2013).

The exact form of the SFR dependence is less clear, but if the fuel for star formation is lower metallicity gas accreted from the IGM, this would produce an anticorrelation between gas phase metallicity and SFR. The form of the secondary dependence of the MZR on SFR offers insights into several open questions, such as how star formation is regulated, and how the processes that govern galactic inflows and outflows operate in detail Davé et al. (2011b,a); Lilly et al. (2013).

In addition to the local MZR and its dependence on SFR, the same correlations can be studied in high redshift galaxies in order to probe galaxy formation and evolution in the early universe (Shapley et al. 2005; Erb et al. 2006; Maiolino et al. 2008; Steidel et al. 2014; Zahid et al. 2014b; Sanders et al. 2015). Furthermore, the correlation between M_* , Z , and SFR in the early universe, and how that relates to the correlations observed in the local universe, constrains how the population of galaxies has evolved over cosmic time (Zahid et al. 2014a; Maier et al. 2014; Izotov et al. 2015).

Accurate and precise metallicity measurements are vital to gain physical insights from both local correlations and evolution over cosmic time. The most reliable oxygen abundances are determined with the “direct method”, or “ T_e method” (Dinerstein 1990). Under the right conditions, the electron temperature of ionized gas can be directly measured from the temperature sensitive intensity ratios of collisionally excited forbidden lines (e.g. [O III] $\lambda 4363$ /[O III] $\lambda 5007$). As oxygen is one of the primary coolants in the ISM, the temperature is anticorrelated with abundance. The density of the gas can be measured from density sensitive lines (e.g. [S II] $\lambda 6717$ / $\lambda 6731$). For a given temperature and density the emissivity of a given ionic species can be computed, which can then be used to determine relative abundances.

The direct method is subject to some biases. Temperature fluctuations and gradients in H II regions produce a bias towards lower metallicities (Peimbert 1967; Kobulnicky et al. 1999). This bias also applies to integrated (as well as stacked) spectra of galaxies. Hotter regions have brighter auroral lines, which can bias the direct method toward higher electron temperatures and correspondingly lower metallicities. Additionally, the assumption of a Maxwell-Boltzmann electron energy distribution has recently come into question (Nicholls et al. 2012; Dopita et al. 2013). If electron energies are instead well described by a κ -distribution, this may contribute to the well known temperature discrepancy problem (García-Rojas & Esteban 2006; García-Rojas & Esteban 2007; Nicholls et al. 2012; Blanc et al. 2015), although this is less of a concern for rel-

ative comparisons of direct method abundances. Even with the potential for these systematic effects, the direct method is widely regarded as the standard for nebular abundances.

In practice, detecting the auroral lines (e.g. [O III] $\lambda 4363$) requires a significant investment of observational resources for even the brightest, most metal poor galaxies and H II regions. At present, most spectroscopy comes from low to moderate SNR, and direct method abundances are typically not practical.

In order to estimate the metallicities of galaxies without the use of the auroral lines, so-called ‘strong-line’ diagnostics were developed based on the more easily measured nebular emission lines (Pagel et al. 1979; Alloin et al. 1979). There have been many efforts to calibrate these diagnostics via theoretical (e.g., McGaugh 1991; Zaritsky et al. 1994; Dopita et al. 2000; Charlot & Longhetti 2001; Kewley & Dopita 2002; Kobulnicky & Kewley 2004; Tremonti et al. 2004; Stasińska 2006) and empirical means (e.g., Pilyugin 2003; Pettini & Pagel 2004; Pilyugin & Thuan 2005; Pilyugin et al. 2010, 2012; Marino et al. 2013; Bianco et al. 2015).

Perhaps the most common of these diagnostics is $R_{23} \equiv ([\text{O II}] \lambda 3727 + [\text{O III}] \lambda \lambda 4959, 5007)/\text{H}\beta$ (Edmunds & Pagel 1984; McCall et al. 1985; Dopita & Evans 1986; Zaritsky et al. 1994). R_{23} encodes some information about the overall oxygen abundance, but the ratio is ultimately determined by the excitation of the [O II] and [O III] lines. This leads to the double valued nature of R_{23} , which complicates its use as an abundance diagnostic.

Fortunately there are other nebular lines that encode information about the gas phase oxygen abundance, and nitrogen is the most accessible of these. Nitrogen has both primary origin, where the amount of nitrogen produced in stars and returned to the ISM is independent of metallicity, and secondary origin, where the amount of nitrogen produced is proportional to metallicity (Alloin et al. 1979; Vila Costas & Edmunds 1993; Considère et al. 2000). In the high metallicity regime, nitrogen is secondary and the nitrogen abundance increases faster than the oxygen abundance. Furthermore, some strong line ratios are temperature sensitive since, for instance, the [O II] $\lambda 3727$ Å line requires a significantly higher energy to excite than the [N II] $\lambda 6583$ Å line (Pilyugin et al. 2010). As a result, nitrogen based diagnostics can serve as indicators of the oxygen abundance.

Many strong-line calibrations are often inconsistent with one another. Kewley & Ellison (2008) show the extent to which the various strong line calibrations disagree and provide a framework for mapping one strong line metallicity onto another. Many of the strong-line calibrations differ simply because they use different calibration samples, but the situation is more complicated than sample selection. Some calibrations utilize grids from photoionization simulations (McGaugh 1991; Zaritsky et al. 1994; Kewley & Dopita 2002), while others use unique samples of H II regions (e.g., Marino et al. 2013) which themselves are often heterogeneous compilations of samples from the literature (e.g., Pettini & Pagel 2004; Pilyugin et al. 2010).

Empirical abundance diagnostics have the benefit of being calibrated on direct method measurements, but due to selection effects the calibration samples are often biased toward low metallicity H II regions (Jones et al. 2015).

The application of these calibrations to integrated spectra of moderately star forming galaxies requires significant extrapolation from the H II regions that compose most calibration samples. Furthermore, most empirical calibrations will result in erroneous metallicities if, for instance, the ionization conditions of the galaxies in question differ significantly from the calibration sample (Dopita et al. 2000; Kewley & Dopita 2002; Steidel et al. 2014).

Recently, several studies have shown that stacking the spectra of a sufficiently large number of galaxies can boost the S/N of the auroral lines to a detectable level (Liang et al. 2007; Andrews & Martini 2013). We use the stacking technique presented in Andrews & Martini (2013) to obtain direct method oxygen abundances for galaxies spanning a wide range in M_* and SFR. Our stacking method mitigates the potential for bias by binning galaxies we expect to have similar metallicities based on the small intrinsic scatter of the MZR and M_*-Z -SFR relation. We then recalibrate the popular strong line abundance diagnostics with the direct method oxygen abundances, and apply the new calibrations to data taken from the literature.

We adopt the following notation for the principal diagnostic emission line ratios:

$$N2 = [\text{N II}] \lambda 6583 / \text{H}\alpha$$

$$O3N2 = [\text{O III}] \lambda 5007 / \text{H}\beta / [\text{N II}] \lambda 6583 / \text{H}\alpha$$

$$N2O2 = [\text{N II}] \lambda 6583 / [\text{O II}] \lambda 3727$$

$$R_2 = [\text{O II}] \lambda 3727 / \text{H}\beta$$

$$R_3 = [\text{O III}] \lambda \lambda 4959, 5007 / \text{H}\beta$$

$$R_{23} = R_2 + R_3$$

$$P = R_3 / R_{23}$$

Section 2 describes our selection and stacking process. Section 3 describes our empirical calibrations of $(\text{O}/\text{H})_{\text{T}_e}$. In Section 4 we present our newly derived calibrations. In Section 5 we apply our calibrations to various samples of galaxies and discuss the implications for the M_*-Z -SFR relation. Finally, we briefly summarize our results in Section 6.

2 DATA

2.1 Sample Selection

Our sample of galaxies is derived from the SDSS Data Release 7 (DR7; Abazajian et al. (2009)). We begin with the MPA/JHU catalog of galaxies with stellar masses (Kauffmann et al. 2003a), SFRs (Brinchmann et al. 2004; Salim et al. 2007), and oxygen abundances (Tremonti et al. 2004, hereafter T04). We discard AGN dominated galaxies with the standard Baldwin-Philips-Terlevich (BPT) diagram (Baldwin et al. 1981) and the criterion for star forming galaxies from Kauffmann et al. (2003b):

$$\log([\text{O III}] \lambda 5007 / \text{H}\beta) < 0.61[\log([\text{N II}] \lambda 6583 / \text{H}\alpha) - 0.05]^{-1} + 1.3. \quad (1)$$

Our S/N requirements are the same as those presented

in Andrews & Martini (2013). We restrict our sample to galaxies with H β , H α , and [N II] $\lambda 6583$ detected at $> 5\sigma$. For galaxies with [O III] $\lambda 5007$ detected at $> 3\sigma$, we apply the selection criteria shown in Equation 1. In order to include galaxies with high metallicity (and inherently weak [O III] $\lambda 5007$) we include galaxies with [O III] $\lambda 5007$ detected at $< 3\sigma$ but $\log([\text{N II}] \lambda 6583 / \text{H}\alpha) < 0.4$.

We also take significant care to inspect low mass galaxies ($\log[M_*] < 8.6$) and remove galaxies with poor photometric deblending (flagged with DEBLEND_NOPEAK or DEBLENDED_AT_EDGE) or otherwise spurious stellar mass determinations. These selection cuts leave a total of 208,529 galaxies in our sample.

We emphasize that a limitation of this analysis is that the data were obtained with single fibers centered on resolved galaxies, and therefore not all of the light is included in the 3'' diameter fiber aperture. For reference, 3'' corresponds to 2.2 kpc at the median redshift ($z = 0.078$) of our sample. The missing fraction due to this aperture bias will depend on redshift for galaxies of similar sizes, and will depend on mass and star formation rate due to the flux-limited nature of the sample. This aperture bias is important because galaxies exhibit radial abundance gradients (e.g. Searle 1971; Kennicutt et al. 2003; Bresolin et al. 2009a,b; Berg et al. 2013; Sánchez et al. 2014) that will cause abundances measured in the central region of a galaxy to overestimate the total abundance. Tremonti et al. (2004) investigated this aperture bias for SDSS observations and found metallicity variations of 0.05 to 0.11 dex with redshift for galaxies of similar absolute z -band magnitudes. Kewley et al. (2005) studied aperture effects with the Nearby Field Galaxy Survey and recommended that fiber spectroscopy include at least $> 20\%$ of the galaxy light (typically $z > 0.04$ for SDSS observations) to minimize systematic and random errors, and this corresponds to most of our sample. Based on these studies, we estimate that aperture biases are comparable to the scatter in the inferred O/H for galaxies of similar stellar mass and star formation rate.

Another limitation of single-fiber observations is they simply present an incomplete picture of the properties of galaxies. One example is that while Sánchez et al. (2013) found a very tight relationship between integrated stellar mass and metallicity with integral field data from CALIFA (Sánchez et al. 2012), they did not find any dependence of metallicity on star formation rate at fixed stellar mass. Another example is the analysis by Belfiore et al. (2015) of nebular data for 14 galaxies with P-MaNGA, the prototype instrument for the ongoing MaNGA survey (Bundy et al. 2015). Those authors found a substantial spread in O/H values at fixed N/O for regions within individual galaxies, which is in contrast to the stronger correlation exhibited by the central regions from single-fiber observations.

2.2 Stacking Procedure

The auroral lines of [N II], [O II], and [O III] are generally weak and typically undetectable in most SDSS galaxy spectra. However, previous studies (e.g. Liang et al. 2007; Andrews & Martini 2013) have demonstrated that stacking spectra to reduce the contribution of random fluctuations in the measured flux is a viable way to obtain sufficient S/N to measure the auroral lines.

The stacking method relies on the fact that the random noise in a composite spectrum of N galaxies scales roughly as $1/\sqrt{N}$; it is advantageous for our bins to contain a large number of galaxies in order to reduce the noise in the spectrum as much as possible. However, we also want each bin to span a very small range in *actual* (O/H) so that we are stacking qualitatively similar galaxies. The chosen bin widths are a compromise between these two goals.

Before stacking the spectra, we follow the same reduction process described in [Andrews & Martini \(2013\)](#). Starting with the spectra that have been processed with the SDSS pipeline ([Stoughton et al. 2002](#)), we correct for Galactic reddening using the extinction values from [Schlegel et al. \(1998\)](#). We then shift each spectrum to the rest frame using redshifts from the MPA/JHU catalog. We interpolate each spectrum onto a wavelength grid spanning 3700Å–7360Å with spacing $\Delta\lambda = 1\text{Å}$. In order to compare galaxies at various distances we normalize each spectrum to the stellar continuum with the mean continuum flux from 4400Å–4450Å. Thus when we measure the line flux we effectively measure the equivalent width of the line. At fixed M_* , normalizing to the stellar continuum is acceptable since the luminosities of the galaxies are essentially the same. Figure 1 demonstrates the benefit of stacking. In the raw SDSS spectrum of a single galaxy (gray line), the weak auroral lines are undetectable. They become fairly evident after stacking (blue line). After removing nearby stellar continuum features (red line), the previously undetectable auroral lines are prominent features in the final spectrum (black line).

2.3 Choice of Stacking Parameters

Our goal is to derive improved strong line calibrations, so one of the parameters we use to assign galaxies to a stack is similar strong line ratios. However, the strong line ratios show considerable dependence on more parameters than just metallicity, such as incident spectral shape, ionization parameter, and gas density ([Dopita et al. 2000](#); [Kewley & Dopita 2002](#); [Dopita et al. 2013](#)). For example, [Steidel et al. \(2014\)](#) demonstrated that variations in line ratios due to a factor of five change in metallicity could be reproduced with only a factor of two change in ionization parameter. Figure 2 clearly demonstrates that there is a substantial range in stellar mass and star formation rate at a constant value of the N2, O3N2, N2O2, or R23 strong line diagnostics.

As in [Andrews & Martini \(2013\)](#), we assume that galaxies with similar stellar masses and star formation rates have similar physical conditions, and therefore similar values of the other parameters that impact the connection between strong line ratio and metallicity. We consequently only stack galaxies with similar stellar masses and star formation rates to minimize the dispersion in galaxy properties in each stack. Good support for this approach comes from an investigation of stacking by [Andrews & Martini \(2013\)](#). They compared electron temperatures and abundances for galaxies with individual auroral line detections to stacks of the same sample of galaxies and found good agreement within the measurement uncertainties.

We have performed a bootstrap analysis as an additional validation of this approach. For this analysis we chose four bins of different star formation rates at the same stel-

lar mass. We resampled each bin 100 times and processed them with our analysis pipeline to derive the metallicity. We found the median of the bootstrap metallicity distribution agreed well with the stack value for each bin. The spread in the metallicity distribution (~ 0.15 dex) was somewhat larger than the formal metallicity uncertainties, but smaller than the variations in the strong line ratios at fixed stellar mass and star formation rate (~ 0.2 dex).

We have chosen to use both stellar mass and star formation rate because there is good evidence that metallicity depends on star formation rate at fixed mass ([Ellison et al. 2008](#); [Mannucci et al. 2010](#); [Lara-Lopez et al. 2010](#)). In addition, we expect galaxies with different star formation rates at fixed mass may differ in other parameters (incident spectral shape, etc.). While the integral field study by [Sánchez et al. \(2013\)](#) did not find that metallicity depends on star formation rate at fixed mass, we emphasize that our decision to stack in both quantities is also motivated by how other physical parameters vary with star formation rate.

It is also well known that stellar mass and star formation rate are well correlated, a correlation known as the star forming main sequence ([Brinchmann et al. 2004](#); [Salim et al. 2007](#); [Noeske et al. 2007](#); [Whitaker et al. 2012](#); [Zahid et al. 2012b](#); [Kashino et al. 2013](#)). In order to characterize this dependence, [Salim et al. \(2014\)](#) showed that the parameter $\Delta \log(\text{SSFR})$

$$\Delta \log(\text{SSFR}) = \log(\text{SSFR}) - \langle \log(\text{SSFR}) \rangle_{M_*} \quad (2)$$

is more effective than both SFR and SSFR at identifying low and high oxygen abundance outliers across a wide range in M_* . The quantity $\langle \log(\text{SSFR}) \rangle_{M_*}$ is the median $\log(\text{SSFR})$ of galaxies at M_* . Thus $\Delta \log(\text{SSFR})$ is defined relative to the star forming main sequence rather than an arbitrary value (e.g. $1 M_\odot \text{ yr}^{-1}$).

Binning in $\Delta \log(\text{SSFR})$ rather than SFR is also beneficial for calibrating the relationship between the strong line ratios and $(\text{O}/\text{H})_{\text{T}_e}$. Figure 2 shows that at a fixed strong line ratio, there is significant scatter in M_* . Since M_* and SFR are correlated, absolute SFR does not necessarily correspond to a lower oxygen abundance at a fixed strong line value. Furthermore, since $\Delta \log(\text{SSFR})$ is a reflection of the SFR density, galaxies with similar $\Delta \log(\text{SSFR})$ ought to have similar ionization conditions. The same does not hold true for galaxies with similar SFR but different stellar masses, since a relatively low mass, compact star forming galaxy will have more intense ionization conditions than a more massive galaxy with relatively diffuse star formation.

Our choice of bin widths was largely *ad hoc*. It is clear from Figure 11 of [Andrews & Martini \(2013\)](#) that there is some scatter in $(\text{O}/\text{H})_{\text{T}_e}$ at fixed M_* and $\Delta \log(\text{SSFR})$. Our primary motives were to (1) resolve the M_* – Z –SFR relationship, (2) include enough galaxies in metal rich stacks to measure $(\text{O}/\text{H})_{\text{T}_e}$, and (3) limit the total number of stacks to keep the stacking procedure, stellar continuum subtraction, and abundance determination computationally feasible. We ran various trials and found our results to be insensitive to bin widths.

The left panel of Figure 3 shows where M_* – $\Delta \log(\text{SSFR})$ stacks fall on the BPT diagram relative to the galaxies in our sample (gray contours) and individual H II regions from [Pilyugin et al. \(2012\)](#) (black points). The stacks with high

$\Delta \log(\text{SSFR})$ are undergoing relatively intense star formation, and their line ratios closely resemble those of individual H II regions. The passively star forming stacks track the overall distribution of galaxies, which is not traced by the individual H II regions.

Naively we expect that galaxies undergoing more intense star formation have many more ionizing photons per atom. While the excitation parameter P is marginally dependant on abundance, the right panel of Figure 3 suggests our naive expectation is correct; stacks with high $\Delta \log(\text{SSFR})$ show systematically higher values of P . Incorporating $\Delta \log(\text{SSFR})$ accounts for some of the strong line ratios' sensitivity to ionization conditions.

Lastly, it is easily shown that many strong line ratios (e.g. N2) are biased by SFR since they include H α flux. By grouping galaxies with similar $\Delta \log(\text{SSFR})$, which is equivalent to SFR at fixed M_* , our chosen stacking methodology minimizes this bias.

2.4 Stellar Continuum Subtraction

Many emission lines used in this study (particularly [O III] $\lambda 4363$) fall in wavelength regimes where stellar absorption features are present. Therefore it is necessary to fit and remove the underlying stellar population contribution to the stacked spectra. Following Andrews & Martini (2013), we use the STARLIGHT spectral synthesis code (Cid Fernandes et al. 2005, 2011) and a library of 300 empirical MILES spectral templates (Sánchez-Blázquez et al. 2006; Cenarro et al. 2007; Vazdekis et al. 2010; Falcón-Barroso et al. 2011) to generate a synthetic spectrum representative of the underlying stellar population for each of our stacks. We adopt the Cardelli et al. (1989) extinction law and mask the locations of all bright emission lines.

For strong lines redward of 4000Å (H β , [O III] $\lambda\lambda 4959, 5007\text{Å}$, H α , [N II] $\lambda\lambda 6548, 6583\text{Å}$, and [S II] $\lambda\lambda 6716, 6731\text{Å}$) we model the stellar continuum using template fits to the entire spectral range (3700Å–7360Å). We fit the continuum near weaker emission lines, auroral lines, and strong lines blueward of 4000Å using template fits to the continuum within a few 100Å of each line since this provides a significant reduction in the rms of the continuum around the line (Andrews & Martini 2013). See Table 1 for details regarding each emission line's fit region.

2.5 Line Flux Measurement

Following Andrews & Martini (2013), we fit the emission lines of the stacked spectra using the *specfit* routine (Kriss 1994) in the IRAF/STSDAS package. We use the simplex χ^2 minimization algorithm to simultaneously fit a flat continuum and Gaussian profile to each emission line. Andrews & Martini (2013) found this to be a robust method consistent with other flux measurement techniques. Uncertainties are derived from the χ^2 of the fit returned by *specfit*. We deredden the spectra using the extinction law from Cardelli et al. (1989) and the assumption of case B recombination (H α /H β = 2.86 for $T_e = 10^4$ K). Andrews & Martini (2013) estimate the systematic error introduced by adopting a fixed H α /H β ratio to be $\lesssim 0.07$ dex. Finally, with the

Table 1. Wavelength Fit and Mask Ranges of Measured Lines.

Line ^a	Fit Range ^b	Mask Range ^c
[O II] $\lambda 3727$	3700–4300	3710–3744
[Ne III] $\lambda 3868$	3800–4100	3863–3873
[S II] $\lambda 4069$	3950–4150	...
H γ $\lambda 4340$	4250–4450	4336–4344
[O III] $\lambda 4363$	4250–4450	4360–4366
He II $\lambda 4686$	4600–4800	4680–4692
[Ar IV] $\lambda 4740$	3700–7360	...
H β $\lambda 4861$	3700–7360	4857–4870
[O III] $\lambda 4959$	3700–7360	4954–4964
[O III] $\lambda 5007$	3700–7360	5001–5013
[N II] $\lambda 5755$	5650–5850	5753–5757
[S III] $\lambda 6312$	6100–6500	6265–6322
[N II] $\lambda 6548$	3700–7360	6528–6608
H α $\lambda 6563$	3700–7360	6528–6608
[N II] $\lambda 6583$	3700–7360	6528–6608
[S II] $\lambda 6716$	3700–7360	6696–6752
[S II] $\lambda 6731$	3700–7360	6696–6752
[Ar III] $\lambda 7135$	7035–7235	7130–7140
[O II] $\lambda 7320$	7160–7360	7318–7322
[O II] $\lambda 7330$	7160–7360	7328–7332

^aEmission lines.

^bThe wavelength range of the stellar continuum fit.

^cThe wavelength range of the stellar continuum fit that was masked out.

Table 2. Line Fluxes

Column	Format	Description
1	F5.2	Lower stellar mass limit of the stack
2	F5.2	Upper stellar mass limit of the stack
3	F5.2	Lower SFR limit of the stack
4	F5.2	Upper SFR limit of the stack
5	I5	Number of galaxies in the stack
6	F8.3	Oxygen abundance of the stack
7	F8.3	Error on oxygen abundance
8	F8.3	[O II] $\lambda 3726$ line flux
9	F8.3	Error on [O 2] $\lambda 3726$ line flux
10	F8.3	[O II] $\lambda 3729$ line flux

(This table is published in its entirety in the electronic edition of the journal. The column names are shown here for guidance regarding its form and content.)

exception of [O II] $\lambda 3727$ Å, our diagnostic emission lines are anchored to nearby Balmer lines, and are thus insensitive to reddening.

3 ANALYSIS

3.1 Abundances

We compute the chemical abundances of the stacks using the same procedure as Andrews & Martini (2013); here we present a brief overview and direct the reader to that paper for further details.

We assume a simple two-zone model composed of a high ionization region (traced by [O III]) and a low ionization region (traced by [O II], [N II], and [S II]). Previous works

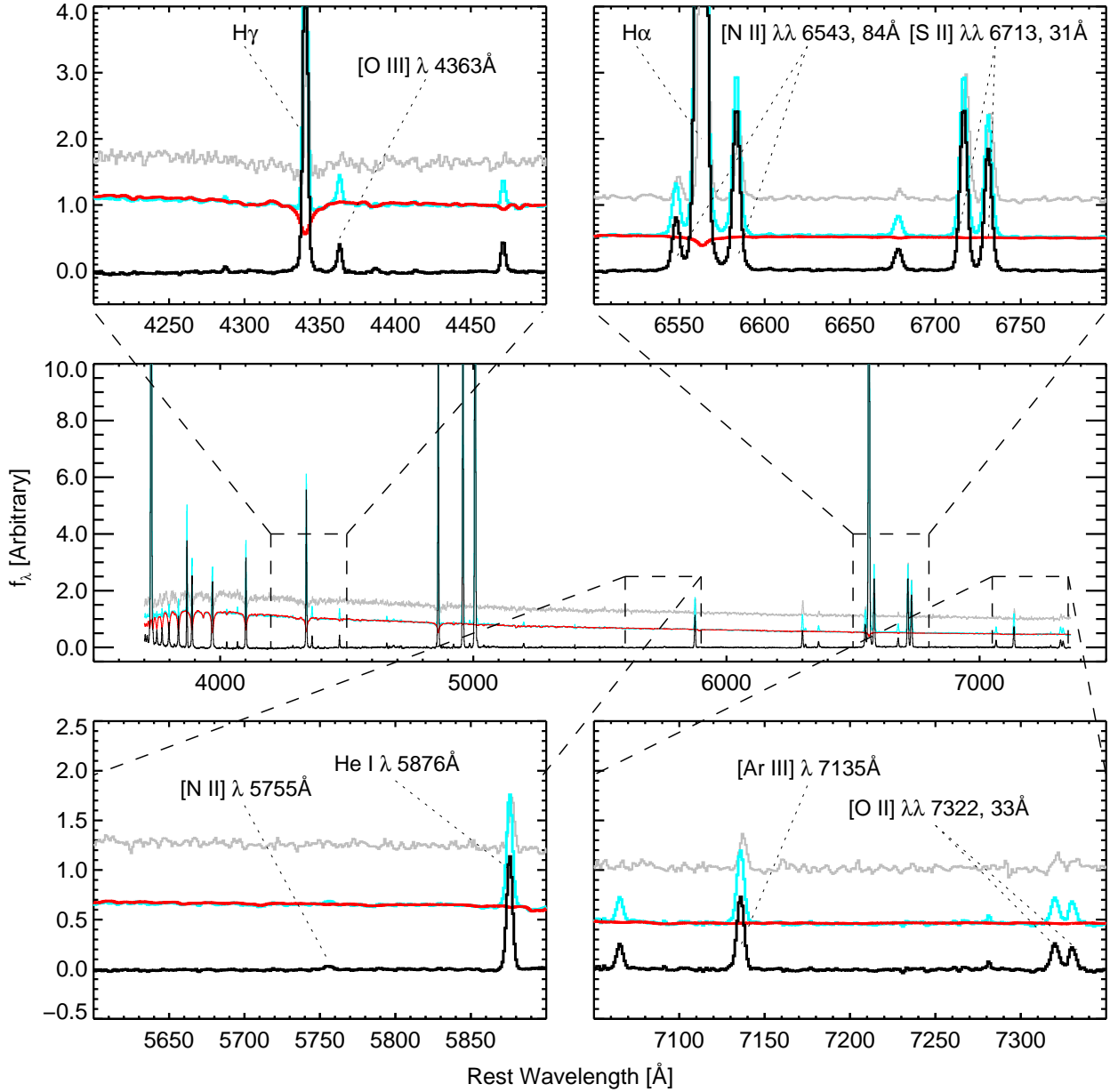


Figure 1. Illustration of how stacking improves the S/N of the weak lines. The top and bottom sets of plots show different regions of the middle spectrum. In each panel, the gray line shows the raw SDSS spectrum (shifted to rest frame wavelength), the blue line shows the stacked spectrum, the red line shows the fit to the stellar continuum, and the thick black line shows the spectrum after stellar continuum subtraction.

have assumed simple relationships between the temperatures of the high and low ionization regions (the $T_2 - T_3$ relation Campbell et al. 1986; Garnett 1992; Pagel et al. 1992; Izotov et al. 2006; Pilyugin et al. 2009). We assume a linear $T_2 - T_3$ relation normalized such that we get the best agreement in stacks for which we are able to measure the temperature of both ionization zones (see below). We use a Monte Carlo technique to derive uncertainties in our measurements.

We measure the electron temperature and density using the IRAF/STSDAS *nebular.temden* routine (Shaw & Dufour 1995), which is based on the 5 level atom from De Robertis et al. (1987). We use the [S II] $\lambda 6717/\lambda 6731$ ratio to measure the electron density. We use the auroral oxygen ratios ($[\text{O II}] \lambda 7320 + 7330 / \lambda \lambda (3726 + 3729)$) and $[\text{O III}] \lambda 4363 / \lambda \lambda (4959 + 5007)$) to measure T_2 and T_3 respectively. Andrews & Martini (2013) discuss at length the differences between the canonical $T_2 - T_3$ relation and that ob-

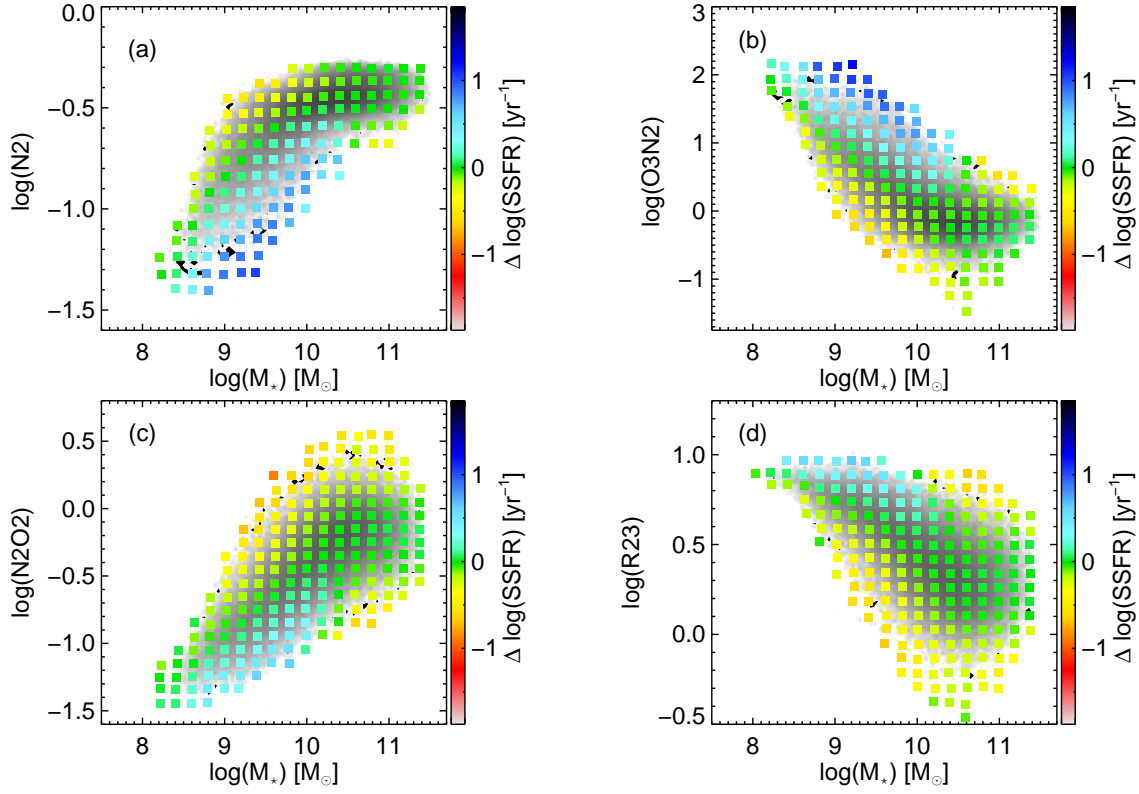


Figure 2. Distribution of SDSS galaxies in the various M_* -diagnostic planes considered here. The individual galaxies are binned in a 2D grid. Color coding denotes the average $\Delta \log(\text{SSFR})$ of each bin; the underlying gray scale shows the relative density of galaxies in our input catalog. Top left to bottom right, the panels show N2, O3N2, N2O2, and R_{23} versus M_* . In the case of N2, O3N2, and N2O2 the scatter in the diagnostic at fixed M_* and $\Delta \log(\text{SSFR})$ is generally small compared to the overall range spanned by the diagnostic. In the case of R_{23} , the distribution of galaxies at fixed M_* and $\Delta \log(\text{SSFR})$ is rather broad compared to the range spanned by the diagnostic, making the R_{23} line ratios of a given stack less meaningful.

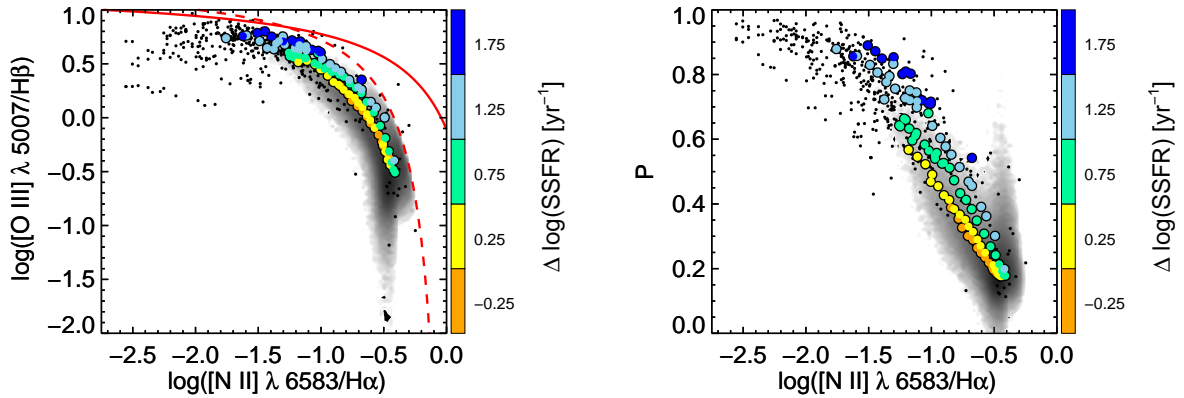


Figure 3. Left: BPT diagram of the stacks (circles) relative to SDSS star forming galaxies (gray contours) and H II regions from Pilyugin et al. (2012) (small black points). Color coding is done according to $\Delta \log(\text{SSFR})$. The dashed and solid red lines are from Kauffmann et al. (2003a) and Kewley et al. (2006) respectively and denote the boundaries between star forming galaxies and AGN. Right: Excitation parameter $P \equiv R_3/R_{23}$ versus $\log(N_2)$. The symbol notation is the same as the left panel. In the high excitation regime, the stacks and SDSS galaxies closely resemble H II regions. At lower excitation (where the majority of SDSS galaxies are located) there are very few H II regions; the two populations are clearly subject to different conditions.

served for their stacks and find that in general their stacks fall below the Campbell et al. (1986) relation (in the sense of low T_2 at fixed T_3). This offset from the predicted relation has been previously seen (Pilyugin et al. 2010). The fact that this offset disappears for galaxies with relatively

high SFRs (which are likely to have contributions from relatively young stellar populations) indicates that the offset is likely due to the differences between the single stellar spectra used by Stasińska (1982) and the composite H II region spectrum that ionizes the gas in a galaxy.

The ionic abundances of O^+ and O^{++} are calculated using the electron temperature, electron density, the flux ratios of the strong lines relative to $H\beta$, and the IRAF/STSDAS *nebular.ionic* routine (De Robertis et al. 1987; Shaw & Dufour 1995). Atomic data plays a critical role in direct method temperature determinations (Kennicutt et al. 2003). For example, Berg et al. (2015) noted a substantial difference in S III temperatures when using updated collision strengths. The O III temperatures are largely unaffected by the updated atomic data, so we utilize the *nebular.temden* routine without modification. The uncertainties in the abundances of individual ionic species are determined with the same Monte Carlo simulations used to determine the uncertainties in electron temperatures. The ionic abundance uncertainties are used to analytically calculate the uncertainty in the total abundances.

We assume the total oxygen abundance is given by

$$\frac{O}{H} = \frac{O^+}{H^+} + \frac{O^{++}}{H^+}. \quad (3)$$

Historically, the temperature of the high ionization region, T_3 , is measured using the direct method and T_2 is then inferred using the $T_2 - T_3$ relation. At high masses, we are unable to measure T_3 but often have a measurement of T_2 . We use the stacks where both T_2 and T_3 are measured to infer a $T_2 - T_3$ relation that results in the best agreement between measured and inferred T_3 . As in Andrews & Martini (2013), this is done using a systematic shift (~ 0.1 dex) in the $\log(O/H)$ of the stacks for which T_2 was measured and used to infer T_3 .

3.2 Empirical Calibrations

There are many abundance diagnostic ratios. Our choice of ratios to consider is motivated by three factors: (1) our calibration(s) should be empirical, (2) the distribution of line ratios for individual galaxies in a stack ought to be reasonably peaked around the mean value, and (3) the calibration ought to be valid for the majority of our stacks.

The most commonly used oxygen abundance diagnostics are N2 and O3N2 (Denicoló et al. 2002; Pettini & Pagel 2004; Marino et al. 2013), N2O2 (Dopita et al. 2000; Kewley & Dopita 2002), and R23 (Pagel et al. 1979; McGaugh 1991; Pilyugin 2003; Kobulnicky & Kewley 2004). Figure 2 shows the distribution of individual galaxies in the M_* -diagnostic planes for these diagnostics. In panel “(a)” of Figure 2, the distribution of galaxies is such that galaxies with similar M_* and $\Delta \log(SSFR)$ follow a relatively tight sequence in the M_* -N2 plane. Similar behavior is seen in panel “(b)” (O3N2) and, to a somewhat lesser extent, panel “(c)” (N2O2). In panel “(d)” at fixed M_* and $\Delta \log(SSFR)$, the values of R_{23} follow a relatively broad distribution; the scatter in R_{23} at fixed M_* and $\Delta \log(SSFR)$ can be comparable to the entire range spanned by the diagnostic. In this instance, the degree to which the average strong line value of a given stack is representative of the galaxies within that stack is less meaningful than with other diagnostics. This is a primary concern when stacking galaxies (see Footnote 14 of Salim et al. (2014) for an example of how binning can lead to the wrong impression).

An additional concern with strong line abundance diagnostics is the effect of ionization parameter variations on

the diagnostic ratios (Kewley & Dopita 2002; Steidel et al. 2014). The ionization parameter Γ is given by

$$\Gamma \equiv \frac{\Phi}{n_H} \approx \frac{\Phi}{n_e} \quad (4)$$

where n_H is the number density of hydrogen atoms and Φ is the density of hydrogen ionizing photons. Changes in the ionization parameter can be due to either variations in the temperature of the ionizing continuum (i.e. a galaxy composed of systematically hotter stars than average) and/or variations in the physical conditions of star forming regions (i.e. higher stellar densities and/or lower gas densities than average). In order to eliminate these biases, it would be advantageous to use a diagnostic that is insensitive to ionization parameter variations (e.g. N2O2, Kewley & Dopita 2002), though our choice of $\Delta \log(SSFR)$ as a second parameter should at least somewhat account for differences in ionization parameter (see the right panel of Figure 3).

The N2 diagnostic is subject to biases caused by the ionization parameter as well as the hardness of the ionization spectrum (Kewley & Dopita 2002), but has been shown to be a useful abundance diagnostic in high excitation regions (Storchi-Bergmann et al. 1994; Binette et al. 1996; Pettini & Pagel 2004; Marino et al. 2013). Furthermore, [N II] λ 6583 and $H\alpha$ are closely spaced, making their ratio insensitive to variations in reddening corrections. The O3N2 diagnostic is also sensitive to ionization parameter (Kewley & Dopita 2002), but is less sensitive to variations in the hardness of the ionizing spectrum than N2 (Kewley et al. 2013; Brown et al. 2014; Steidel et al. 2014). N2O2 is insensitive to ionization parameter, but is dependent on the secondary nature of nitrogen (Kewley & Dopita 2002). We will use N2O2 to estimate the effect of ionization parameter variations on the other diagnostics.

With the above considerations in mind, we focus the remainder of our analysis on the N2, O3N2, and N2O2 strong line diagnostics. As discussed above, the distribution of R_{23} at fixed M_* and $\Delta \log(SSFR)$ is not strongly peaked. Furthermore, the double valued nature of R_{23} requires that an additional diagnostic sensitive to ionization parameter be used in conjunction with an iterative method to solve for an oxygen abundance. This precludes the empirical nature of our calibrations. Most importantly, a large fraction of our galaxies fall within the “transition zone” of the R_{23} diagnostic, where the diagnostic is insensitive to oxygen abundance (Dopita et al. 2013). As a result, we refrain from further consideration of R_{23} .

4 RESULTS

In Section 2.3 we demonstrated with Figure 2 that each M_* - $\Delta \log(SSFR)$ stack has characteristic diagnostic line ratios which are representative of the individual galaxies in that stack. Following previous works (e.g., Alloin et al. 1979; Pettini & Pagel 2004; Marino et al. 2013) we combine these diagnostic ratios with direct method oxygen abundances to derive a relationship between the two. Salim et al. (2014) showed that at fixed M_* we expect galaxies with low (high) $\Delta \log(SSFR)$ to be offset from the star forming main sequence in the sense of high (low) oxygen abundance. Given the strong correlation between our diagnostic ratios and M_* ,

we assume the following form for our empirical calibrations:

$$12 + \log(\text{O}/\text{H}) = f_1(X) + f_2(\Delta \log(\text{SSFR})) \quad (5)$$

where X is a particular diagnostic value (e.g. N2) and f_1 and f_2 are functions of the respective variables. For simplicity, we assume f_1 and f_2 are each linear functions in their respective parameter, except for the case of N2 where we allow f_1 to take the form of a second degree polynomial. We use MPFIT (Markwardt 2009), an IDL implementation of the robust non-linear least square fitting routine MINPACK-1, to fit the relationship between $\log(\text{O}/\text{H})$, X , and $\Delta \log(\text{SSFR})$.

From Equation 2, it is clear that for a galaxy with a known M_* and SFR, $\Delta \log(\text{SSFR})$ then only depends on the average SSFR at that M_* . In practice, we compute the median SSFR in M_* bins 0.1 dex wide. However, a good approximation for $\langle \log(\text{SSFR}) \rangle_{M_*}$ as a function of M_* is:

$$\begin{aligned} \langle \log(\text{SSFR}) \rangle_{M_*} = & 283.728 - 116.265 \times \log M_* + \\ & 17.4403 \times \log M_*^2 - 1.17146 \times \log M_*^3 + 0.0296526 \times \log M_*^4. \end{aligned} \quad (6)$$

We provide this form rather than the expression from Salim et al. (2007) because the two begin to diverge below $\log(M_*/M_\odot) \sim 9$.

4.1 N2 Method

Our new calibration of $(\text{O}/\text{H})_{\text{T}_e}$ based on N2 and $\Delta \log(\text{SSFR})$ is

$$12 + \log(\text{O}/\text{H})_{\text{N2}} = 9.12 + 0.58 \times \log(\text{N2}) - 0.19 \times \Delta \log(\text{SSFR}). \quad (7)$$

Figure 4 shows that the slope of the relationship between $(\text{O}/\text{H})_{\text{T}_e}$ and N2 at fixed $\Delta \log(\text{SSFR})$ is comparable to the slope of Pettini & Pagel (2004) (red line) and Marino et al. (2013) (magenta line), and agree well for the galaxies with high $\Delta \log(\text{SSFR})$. This agrees with previous studies (e.g. Brown et al. 2014) which have shown that those empirical relations accurately predict $(\text{O}/\text{H})_{\text{T}_e}$ for high excitation galaxies. This is not particularly surprising because galaxies with very compact, high star formation rates for a given M_* are similar to individual H II regions in terms of excitation conditions.

As one moves from high excitation galaxies toward the star forming main sequence, the population of galaxies tends toward lower excitation conditions than the H II regions used in Pettini & Pagel (2004). The observational consequence is that SDSS galaxies have higher $(\text{O}/\text{H})_{\text{T}_e}$ than predicted by previous calibrations at a given value of N2.

For galaxies above $\sim Z_\odot$, N2 saturates as it becomes the dominant coolant of the ISM (Baldwin et al. 1981; Pettini & Pagel 2004). This explains the pile up of stacks around $\log(\text{N2}) \approx -0.5$ in Figure 4 for the low $\Delta \log(\text{SSFR})$ stacks. As a result this calibration becomes unreliable when the line ratio reaches this value. The top panel of Figure 4 shows the residuals of the fit. It is clear that the quality of the calibration worsens at high metallicities. We include the RMS of the residuals in Table 3.

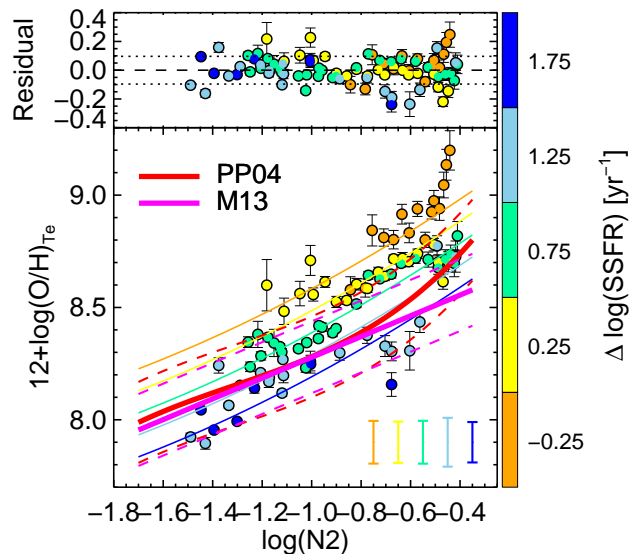


Figure 4. Direct method oxygen abundances of the stacks as a function of N2 and $\Delta \log(\text{SSFR})$. The circles show the actual measurements; the various lines show our fit to $(\text{O}/\text{H})_{\text{T}_e}$ as a function of N2 and $\Delta \log(\text{SSFR})$. The thick red and magenta lines show the fits from Pettini & Pagel (2004) and Marino et al. (2013), respectively, which are based almost entirely on direct method oxygen abundances of individual H II regions. The top panel shows the residuals of the fit; the dashed lines show the RMS of the residuals.

4.2 O3N2 Method

Our new calibration of $(\text{O}/\text{H})_{\text{T}_e}$ based on O3N2 and $\Delta \log(\text{SSFR})$ is

$$12 + \log(\text{O}/\text{H})_{\text{O3N2}} = 8.98 - 0.32 \times \log(\text{O3N2}) - 0.18 \times \Delta \log(\text{SSFR}). \quad (8)$$

Figure 5 shows that the slope of the relationship between $(\text{O}/\text{H})_{\text{T}_e}$ and O3N2 at fixed $\Delta \log(\text{SSFR})$ is comparable to the slope of Pettini & Pagel (2004) (thick red line) and Marino et al. (2013) (thick magenta line), and agrees well for the galaxies with high $\Delta \log(\text{SSFR})$. Again this is in agreement with Brown et al. (2014), who showed that high excitation galaxies with significant populations of young stars are essentially indistinguishable from individual H II regions from the perspective of a diagnostic ratios. We do find a marginally steeper slope than Marino et al. (2013). This could be due to a selection effect because at high (low) metallicities we lack high (low) $\Delta \log(\text{SSFR})$ bins, which could artificially steepen our calibration. In addition, the steepness of the Pettini & Pagel (2004) calibration may be due to the photoionization models used at high metallicities. The Marino et al. (2013) calibration suffers no such bias, since their measurements are based entirely on individual H II regions. More data are needed to explore this possibility further.

Closer to the star forming galaxy main sequence, the calibration presented here begins to diverge from the previous calibrations based on H II regions. Again, this is because the galaxies on the star forming main sequence display lower

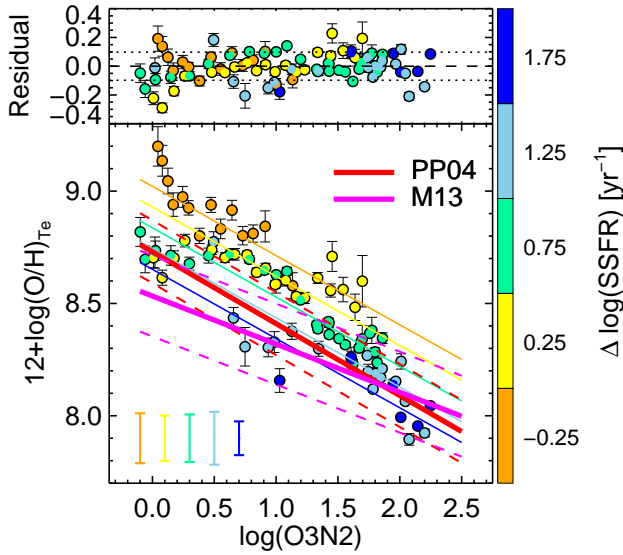


Figure 5. Same as Figure 4 but for the O3N2 diagnostic.

excitation conditions than the H II regions used in the previous calibrations.

The O3N2 diagnostic performs better than the N2 diagnostic at high $(O/H)_{Te}$. While N2 saturates at high metallicity, the intensity of collisionally excited oxygen lines is still falling with increasing oxygen abundance.

4.3 N2O2 Method

Our new calibration of $(O/H)_{Te}$ based on N2O2 and $\Delta \log(SSFR)$ is

$$12 + \log(O/H)_{N2O2} = 9.20 + 0.54 \times \log(N2O2) - 0.36 \times \Delta \log(SSFR). \quad (9)$$

In Figure 6 we compare our measurements from the stacks with the N2O2 calibration from Kewley & Dopita (2002). At high metallicities, we find excellent agreement between the star forming galaxy main sequence of our stacks and the calibration from Kewley & Dopita (2002). This could be due to the fact that this calibration is insensitive to ionization parameter. At fixed N2O2, stacks with high $\Delta \log(SSFR)$ show lower $(O/H)_{Te}$ than stacks with lower $\Delta \log(SSFR)$, as one would expect in the case of inflow driven star formation.

Kewley & Dopita (2002) explicitly state that the N2O2 calibration should only be used above $12 + \log(O/H) > 8.6$ since this diagnostic derives its utility from the secondary nature of nitrogen at high metallicity. However, in the context of galaxy evolution where inflows and outflows have a strong effect on the oxygen abundance we argue that this selection criteria should instead be based on the value of the N2O2 diagnostic itself. For instance, consider a galaxy which has undergone prolonged star formation and enriched its ISM well above solar metallicity such that the secondary nature of nitrogen is unambiguous. Now, suppose this galaxy were to accrete a substantial amount of gas from

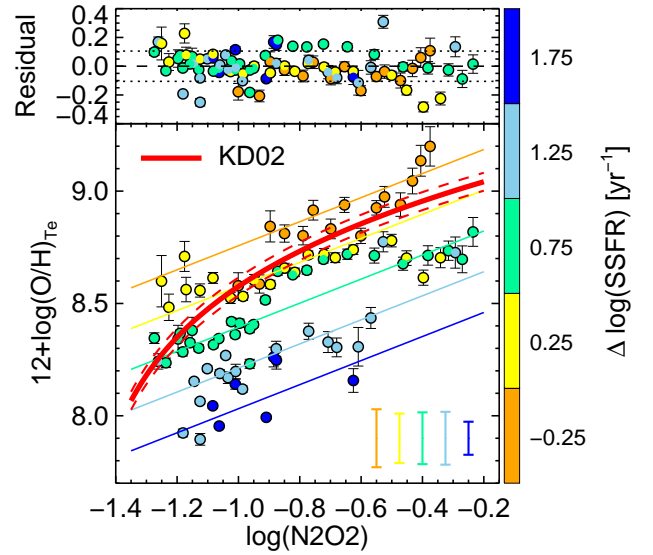


Figure 6. Same as Figure 4 but for the N2O2 diagnostic. The thick red line shows the fit from Kewley & Dopita (2002).

the IGM. The ISM would be diluted, the metallicity would decrease, and the SFR would increase. The galaxy would move off the main sequence, increasing $\Delta \log(SSFR)$. All the while, the N2O2 ratio would remain largely unchanged, since the relative abundance of nitrogen and oxygen is unaffected by inflows of pristine gas (Köppen & Hensler 2005; Masters et al. 2014). The high SFR stacks shown in Figure 14 of Andrews & Martini (2013) are consistent with this picture of inflow driven dilution. Nitrogen can be secondary even at low metallicities, provided the galaxy is sufficiently chemically evolved.

Figure 3 of Kewley & Dopita (2002) shows that the N2O2 diagnostic becomes sensitive to metallicity at $\log(N2O2) \sim -1.25$. Our Figure 6 illustrates that this happens at the lower range probed by our stacks. The $(O/H)_{Te}$ of our stacks does show a clear dependence on N2O2, even at low metallicities. Unevolved galaxies for which nitrogen is still primary could potentially contaminate the stacks. However, the left panel of Figure 2 shows that there are relatively few galaxies with $\log(N2O2) < -1.25$. Thus we are confident our N2O2 calibrations are valid even though we apply them at low metallicities.

4.4 Which Calibration Is Best?

Figure 7 summarizes our results in $M_* - \Delta \log(SSFR)$ space and illustrates several systematic effects correlated with M_* and/or $\Delta \log(SSFR)$.

The top panel shows the distribution of stacks with measured $(O/H)_{Te}$ in $M_* - \Delta \log(SSFR)$ space. The color of each square reflects the metallicity. The second, third, and fourth panels show the residuals for the N2, O3N2, and N2O2 diagnostics, respectively. Red indicates where the strong line diagnostic overestimates the direct method metallicity, while blue indicates the alternative. Column d in Table 3 shows the mean residuals for each calibration. On average the calibrations are accurate to within 0.10 dex, al-

Table 3. Calibration results.

Diagnostic	a	b	c	d	rms Residuals
N2.....	9.25	0.83	0.12	-0.20	0.0965
O3N2.....	8.98	-0.32	...	-0.18	0.0976
N2O2.....	9.20	0.54	...	-0.36	0.1053
Star Forming Main Sequence					
$\langle \log(\text{SSFR}) \rangle_{M_*} = 283.728 - 116.265 \times \log M_* + 17.4403 \times \log M_*^2 - 1.17146 \times \log M_*^3 + 0.0296526 \times \log M_*^4$					

though there are typically 2-3 stacks for each diagnostic that have substantially larger residuals. The calibrations perform worse for the highest metallicity stacks. This is evident in residuals shown in the top panels of Figures 4, 5, and 6. The metallicities of the lowest mass stacks are also difficult to accurately predict. This is likely due to the small number (~ 5) of galaxies in these stacks. One or two galaxies with anomalous line ratios can significantly influence the line ratios of the stack (Andrews & Martini 2013).

In general, no single calibration vastly outperforms the others, though O3N2 does fare slightly better. O3N2 was the preferred diagnostic for 43% (47/110) of the stacks, followed by N2O2 with 30% (33/110), and N2 was ranked last with 27% (30/110). There does not appear to be any systematic trend where one calibration does better than the others, though N2O2 is only marginally worse than O3N2 for many of the stacks and is subject to fewer biases.

The N2O2 calibration has a larger dependence on $\Delta \log(\text{SSFR})$ (0.36, column d in Table 3) than the other calibrations (~ 0.2). This likely reflects the fact that N2 and O3N2 are sensitive to ionization parameter, whereas N2O2 is not. At fixed metallicity, a systematically high ionization parameter (correlated with high $\Delta \log(\text{SSFR})$) biases the N2 and O3N2 line ratios in the direction of low metallicity. Thus stacks with high $\Delta \log(\text{SSFR})$ have metal poor line ratios relative to a stack of lower $\Delta \log(\text{SSFR})$ and identical metallicity. This reduces the inferred dependence of metallicity on $\Delta \log(\text{SSFR})$. While all three calibrations perform equally well for our sample, these biases may be important considerations for applications to other samples. We emphasize that the rms residuals of the fit to the stacks does not reflect the actual precision of the calibration. As noted in Section 2.3, the reliability of the calibrations is primarily determined by the scatter in a given line ratio at fixed M_* and $\Delta \log(\text{SSFR})$, which is assumed to mean fixed O/H. This scatter is ultimately a function of M_* , SFR, strong-line diagnostic, and sample selection. We include error bars in the lower corners of Figures 4, 5, and 6 to show the typical uncertainty for our different $\Delta \log(\text{SSFR})$ bins, marginalized over M_* . The error bars (~ 0.2 dex) reflect the uncertainty in inferred O/H due to the scatter in strong-line ratio at fixed M_* and $\Delta \log(\text{SSFR})$, and typically exceed the widths of the O/H distributions in our bootstrap analysis (~ 0.15 dex).

5 DISCUSSION

5.1 Application of New Calibrations to Local Galaxies

We first apply our newly derived strong line calibrations to the sample of individual star forming galaxies that went into our stacks. In Figures 8, 9, and 10 we show the distribution of SDSS galaxies (gray contours) and $M_* - \Delta \log(\text{SSFR})$ stacks (colored points) in the M-Z plane. All metallicities are computed using the appropriate strong line calibration. In Figure 8 we apply the N2 calibration, in Figure 9 we apply the O3N2 calibration, and in Figure 10 we apply the new N2O2 calibration. In each panel the solid (dotted) red lines show the appropriate best fit MZR (scatter) from Kewley & Ellison (2008), in which the MZRs were measured by computing the median $\log(\text{O}/\text{H})$ as a function of mass. The dot-dashed magenta lines show the MZR from Tremonti et al. (2004).

If each $M_* - \Delta \log(\text{SSFR})$ bin has a known $(\text{O}/\text{H})_{\text{Te}}$, the uncertainty in the calibration is dominated by the average scatter in a given diagnostic at fixed $(\text{O}/\text{H})_{\text{Te}}$. The error in any given measurement of $(\text{O}/\text{H})_{\text{Te}}$ is typically much smaller than this. We estimate the scatter in a diagnostic at fixed $(\text{O}/\text{H})_{\text{Te}}$ by averaging the scatter in the diagnostic over all masses at fixed $\Delta \log(\text{SSFR})$. These uncertainties are shown as error bars in the bottom corner of the plots and are generally comparable to the uncertainties in the calibrations (~ 0.10 dex). The error bars on the points themselves represent the error on the mean. Due to the large number of galaxies in most stacks, the mean is typically measured to high precision.

In the case of N2 and O3N2, we find that our direct method strong line calibrations produce MZRs with higher (O/H) normalizations than the Kewley & Ellison (2008) results, as expected from Figures 4 and 5. In the case of N2O2, the normalization of the MZR is only marginally higher than the results from Kewley & Ellison (2008); this is due to the fact that, without accounting for $\Delta \log(\text{SSFR})$, our N2O2 calibration is very similar to that presented in Kewley & Dopita (2002). The slopes of all of our MZRs are roughly consistent with the results from Kewley & Ellison (2008) and also appear to flatten at low masses ($\log(M_*) \lesssim 8$). Each of the MZRs also agree well with the Tremonti et al. (2004) MZR.

Figures 4 and 5 suggest that the $\Delta \log(\text{SSFR})_{1.0}^{1.5}$ bins should follow the Kewley & Ellison (2008) MZR closest, when in fact it is the $\Delta \log(\text{SSFR})_{0.5}^{1.0}$ bins. This is purely a selection effect due to the difference in binning schemes. Kewley & Ellison (2008) effectively binned in M_* , whereas

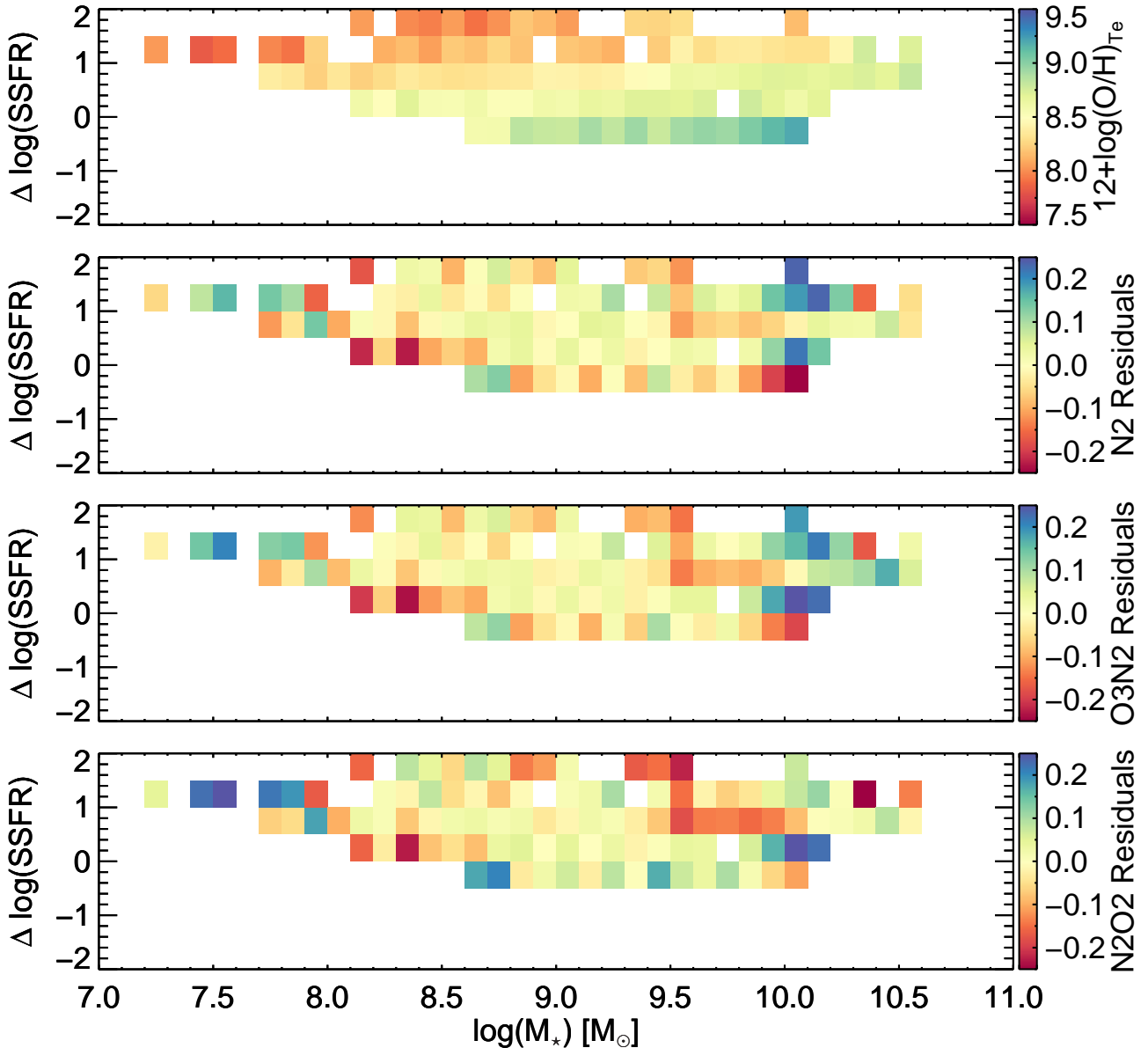


Figure 7. Overview of our binning and quality of our strong-line calibrations. The top panel shows the distribution of direct method measurements in M_* - $\Delta \log(\text{SSFR})$ space. Each square represents a M_* - $\Delta \log(\text{SSFR})$ stack. The color coding denotes metallicity. Metallicity generally increases as M_* increases and/or $\Delta \log(\text{SSFR})$ decreases. The second, third, and fourth panels show the residuals for the N2, O3N2, and N2O2 diagnostics respectively. All three diagnostics perform well across most of the parameter space. The O3N2 diagnostic was the most accurate (47/110 bins), followed by N2O2 (33/110 bins) and N2 (30/110 bins).

we have binned in both M_* and $\Delta \log(\text{SSFR})$. As shown in Figure 2 (top left), the M_* - $\Delta \log(\text{SSFR})$ stacks with high $\Delta \log(\text{SSFR})$ have lower values of N2 than a corresponding mass stack. This is primarily because at fixed M_* , higher $\Delta \log(\text{SSFR})$ implies higher $\text{H}\alpha$ flux, and thus lower N2. The reason we bin in M_* and $\Delta \log(\text{SSFR})$ is to alleviate the dependence of N2 on $\Delta \log(\text{SSFR})$; the difference between our results and those of Kewley & Ellison (2008) effectively reveal the magnitude of this bias.

We find that the N2 MZR (Figure 8) asymptotes around solar metallicity and falls slightly below the MZR from Tremonti et al. (2004). This is in agreement with previous studies (Baldwin et al. 1981; Pettini & Pagel 2004) and oc-

curs because nitrogen becomes the dominant coolant at high metallicity, so N2 saturates. At high stellar masses (and metallicities), O3N2 continues to decrease as the intensity of [O III] decreases with increasing metallicity. Figures 2 and 9 show that O3N2 begins to flatten at high M_* , but this is likely due to the turnover in the MZR.

In the case of the N2O2 MZR (Figure 10), we note a marginally higher normalization, and significantly larger scatter at fixed M_* , than the other calibrations. This is likely the result of a larger dependence on $\Delta \log(\text{SSFR})$. As previously noted, the ionization parameter is likely correlated with $\Delta \log(\text{SSFR})$ (see the right panel of Figure 3). If this is true, the high $\Delta \log(\text{SSFR})$ stacks will be biased towards

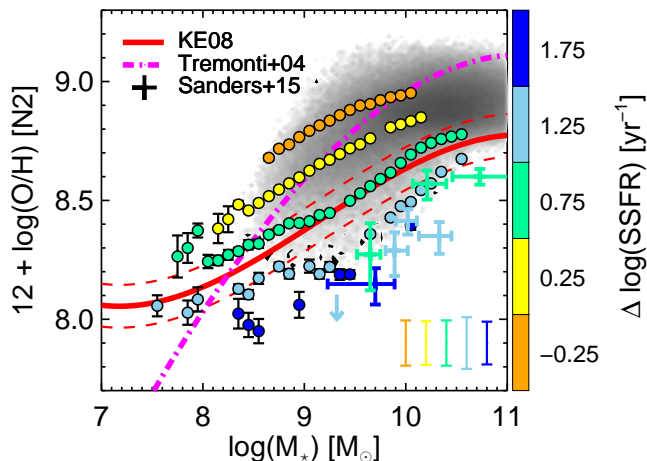


Figure 8. The MZR derived with our new N2 calibration. The circles represent our stacks, the crosses represent the high redshift star forming galaxy stacks from Sanders et al. (2015), and the gray contours represent the star forming SDSS galaxies used in our analysis. The thick red line shows the mass binned results from Kewley & Ellison (2008). The dot-dashed magenta line shows the MZR from Tremonti et al. (2004). The smooth behaviour of the stacks is ultimately the result of the average N2 varying so smoothly with M_* . The galaxies from Sanders et al. (2015) display lower (O/H) than the stacks with comparable M_* and $\Delta \log(\text{SSFR})$.

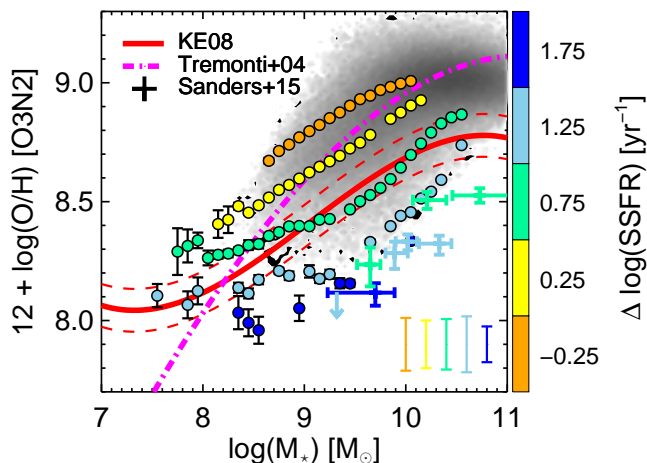


Figure 9. Same as Figure 8 but using the O3N2 diagnostic.

low N2 or high O3N2 (Dopita et al. 2000; Kewley & Dopita 2002; Steidel et al. 2014). Given the slope of the strong line calibrations, this will mask the dependence of $\log(\text{O}/\text{H})$ and $\Delta \log(\text{SSFR})$. Being largely insensitive to ionization parameter, N2O2 likely reflects the true relationship between $\log(\text{O}/\text{H})$ and $\Delta \log(\text{SSFR})$.

For most of the $\Delta \log(\text{SSFR})$ tracks, the scatter in inferred (O/H) between points is surprisingly small and is much less than that seen in $(\text{O}/\text{H})_{\text{T}_e}$. This is due to the fact that the inferred (O/H) is merely a reflection of how the strong line diagnostics vary as a function of mass. On average, the strong lines exhibit very smooth behavior with

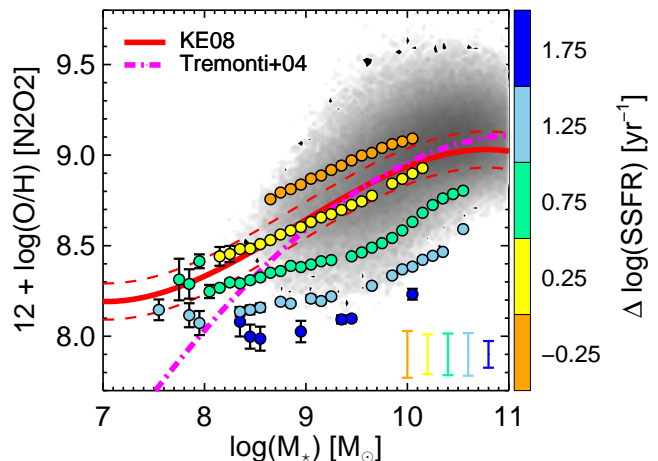


Figure 10. Same as Figure 8 but for the N2O2 diagnostic. The high redshift star forming galaxy stacks from Sanders et al. (2015) are not included here, as the $[\text{O II}] \lambda 3727 \text{ \AA}$ line does not fall within the spectral range of the MOSFIRE instrument at $z \sim 2.3$. Note that the MZR resulting from this calibration has a higher normalization and larger scatter at fixed M_* than the other calibrations.

mass (Kewley & Ellison 2008). This point was also raised in Steidel et al. (2014) and suggests that another parameter other than gas phase oxygen abundance (likely ionization parameter) is tightly coupled to both mass and the strong line ratios. Thus we are able to measure the average strong line value to exquisite precision, but the uncertainty in gas phase oxygen abundance for any one galaxy is set by the scatter in a particular diagnostic ratio at fixed M_* and $\Delta \log(\text{SSFR})$.

5.2 The M_* -Z-SFR Relation

Using the masses and newly derived oxygen abundances of galaxies in the local universe, we can investigate the presence of a Fundamental Metallicity Relation (FMR; Mannucci et al. (2010); Lara-López et al. (2010)). The formulation of the FMR from Mannucci et al. (2010) states that (1) galaxies lie along the projection of the local M_* -Z-SFR relation that minimizes the scatter in metallicity, and (2) the relationship is redshift invariant. In this section we will focus on the first of these predictions; we will consider evolution of the M_* -Z-SFR relation with redshift in Section 5.3.

Salim et al. (2014) presented a non-parametric analysis framework for investigating the M_* -Z-SFR relation in local galaxies. When investigating the nature of the M_* -Z-SFR relation, non-parametric techniques are preferred since they do not require a fixed SFR dependence at a given M_* , as is required in the framework of Mannucci et al. (2010) or Lara-López et al. (2010). Following Salim et al. (2014, 2015), we examine the slope of $12 + \log(\text{O}/\text{H})$ as a function of $\Delta \log(\text{SSFR})$ at fixed M_* . For each M_* bin, we assume the form

$$12 + \log(\text{O}/\text{H}) = \beta + \kappa * \Delta \log(\text{SSFR}). \quad (10)$$

While this introduces a parametrization, it allows for a

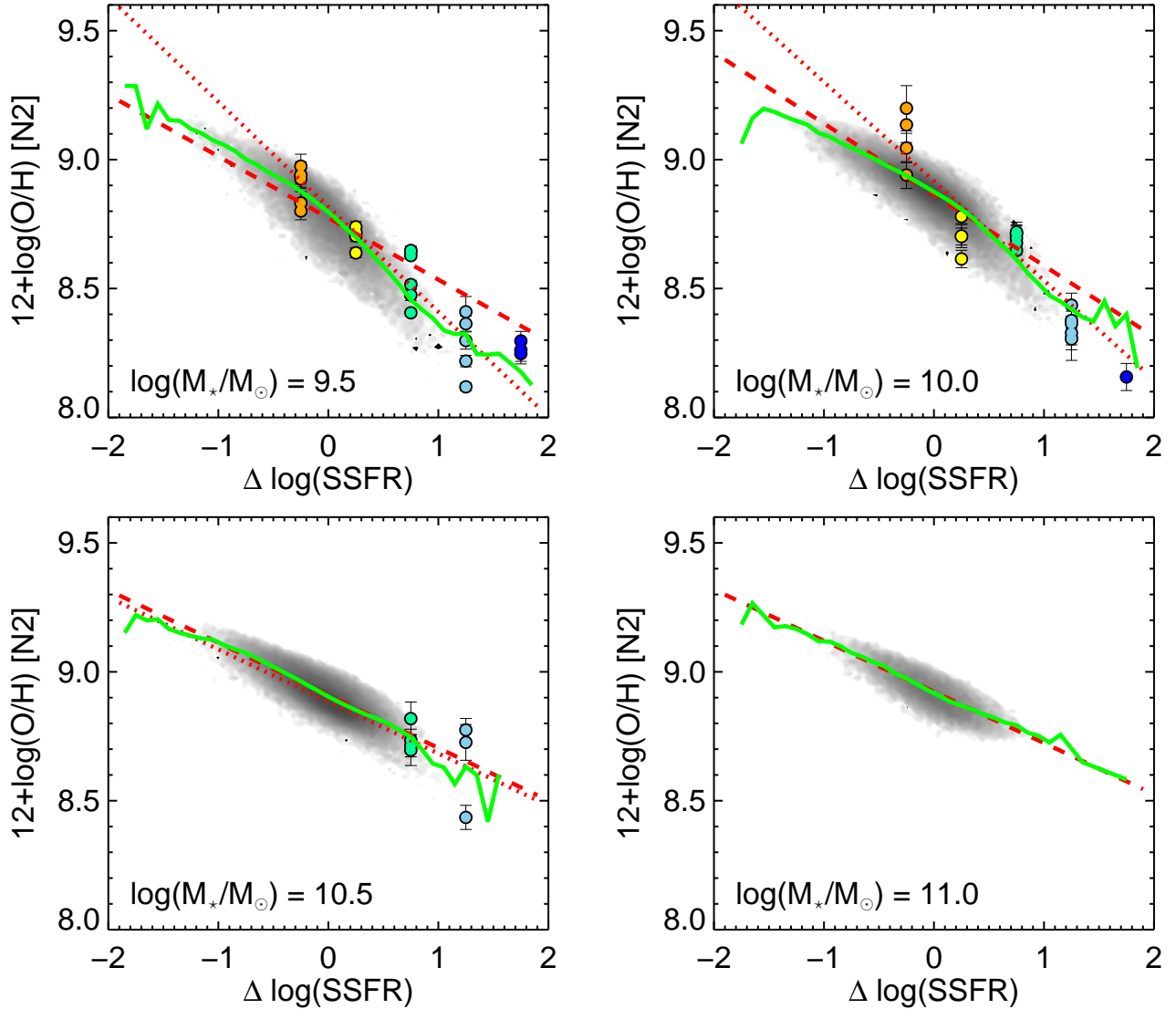


Figure 11. Oxygen abundance as a function of $\Delta \log(\text{SSFR})$ for the N2 calibration. Each panel shows galaxies and stacks falling within ± 0.25 dex of the designated mass. The gray contours show the distribution of SDSS galaxies; the circles show the stacks falling within the designated mass range (there are often multiple stacks at a given value of $\Delta \log(\text{SSFR})$). The color coding denotes $\Delta \log(\text{SSFR})$. Oxygen abundances of the individual galaxies are derived from our new N2 calibration; oxygen abundances of the stacks are derived from the direct method. In each panel, the solid green line shows the median of the individual galaxies, the dashed red line shows the linear fit to the individual galaxies, and the dotted red line shows the linear fit to the stacks. Selection effects cause (1) a reduction in the number of direct method measurements at high M_* , and (2) the fit to the stacks to be biased towards a steeper slopes. This latter effect is due to the fact that the direct method abundances are more easily measured at high $\Delta \log(\text{SSFR})$, where the relation between $\log(\text{O}/\text{H})$ and $\Delta \log(\text{SSFR})$ tends to steepen. The nonlinear nature of the green line illustrates the need for such a non-parametric approach. The corresponding plots for the O3N2 diagnostic (not shown) are qualitatively similar to those shown here.

direct comparison of the slope κ with previous studies (e.g. Salim et al. 2014, 2015). The dependence of $\log(\text{O}/\text{H})$ on SFR at fixed M_* is simply $\left. \frac{d \log(\text{O}/\text{H})}{d \log(\text{SFR})} \right|_{M_*} = \frac{d \log(\text{O}/\text{H})}{d \Delta \log(\text{SSFR})} = \kappa$. This differs from the parameter α that minimizes the scatter about a surface in M_* - Z -SFR space (e.g., Mannucci et al. 2010; Yates et al. 2012; Andrews & Martini 2013). It is straightforward to convert a value of α to an equivalent value of κ if the parametrization of the FMR is known.

Salim et al. (2014) find that the slope κ is a function of M_* , and becomes flatter at higher masses. They also find that the slope is a function of $\Delta \log(\text{SSFR})$, and becomes steeper at higher $\Delta \log(\text{SSFR})$. We apply their framework to

the galaxies in our sample. We measure $\Delta \log(\text{SSFR})$ with Equation 2, and apply our new strong line calibrations to derive oxygen abundances.

Each panel of Figure 11 shows $\log(\text{O}/\text{H})$ as a function of $\Delta \log(\text{SSFR})$ for a given M_* denoted in the bottom left corner. We include all galaxies and stacks with masses that fall within the ± 0.25 dex M_* window of each panel. The circles show the direct method abundances of the stacks. The stacks are 0.10 dex wide in M_* , so there are multiple stacks at fixed $\Delta \log(\text{SSFR})$ within the M_* window of each panel. The gray contours show the SDSS galaxies with oxygen abundances determined with our new calibration.

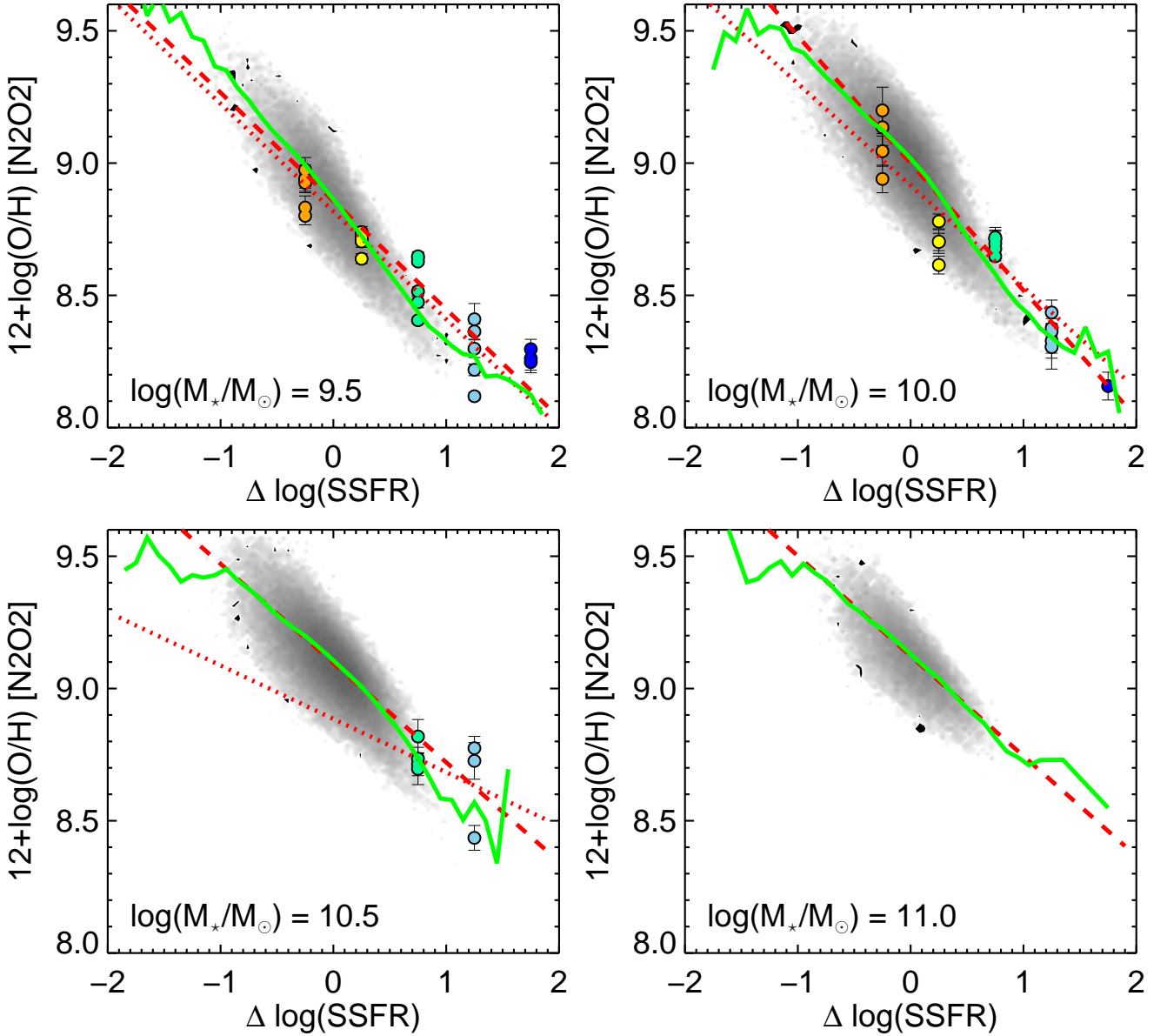


Figure 12. Same as Figure 11 but using the N2O2 diagnostic. The dependence on $\Delta \log(\text{SSFR})$ is generally steeper than that of the N2 and O3N2 diagnostics, even at high masses. The dependence is also well approximated with the linear parametrization.

For each M_* , we fit $\log(\text{O}/\text{H})$ as a function of $\Delta \log(\text{SSFR})$ per Equation 10. The dashed red lines show the fits resulting from the SDSS galaxies; the dotted red lines show the fits to the stacks. Note that for higher masses ($\log(M_*/M_\odot) \gtrsim 10.0$) there are few to no stacks with direct method abundances. While in some cases the slopes derived from the direct method differ from those derived from the individual galaxies (e.g., $\log(M_*/M_\odot) = 9.5$), we typically find agreement within the error bars.

The solid green line in each panel shows the median $\log(\text{O}/\text{H})$ as a function of $\Delta \log(\text{SSFR})$. The relationship between $\log(\text{O}/\text{H})$ and $\Delta \log(\text{SSFR})$ is non-linear and appears to steepen at high $\Delta \log(\text{SSFR})$, particularly for the lower mass bins. This is in agreement with Salim et al. (2014) and illustrates the need for a non-parametric approach when investigating the M_* - Z -SFR relation. Since our detection

of auroral lines is biased towards high $\Delta \log(\text{SSFR})$, we have relatively more direct method measurements at high $\Delta \log(\text{SSFR})$, which effectively biases the fit to the stacks towards a steeper slope. Accounting for $\Delta \log(\text{SSFR})$ does lead to a reduction in scatter; the scatter in (O/H) at fixed M_* and $\Delta \log(\text{SSFR})$ is somewhat lower than the scatter at fixed M_* alone. In the case of N2, the scatter in O/H at fixed M_* is ~ 0.12 , while the scatter around the running median is 0.07.

We perform this analysis for the O3N2 and N2O2 diagnostics as well. The results for the O3N2 diagnostic are qualitatively similar to those of the N2 diagnostic. In Figure 12 we examine the results of this non-parametric approach with the N2O2 diagnostic. The green line shows the median $\log(\text{O}/\text{H})$ of the individual galaxies, while the dashed (dotted) red lines show the parametrized fit to the

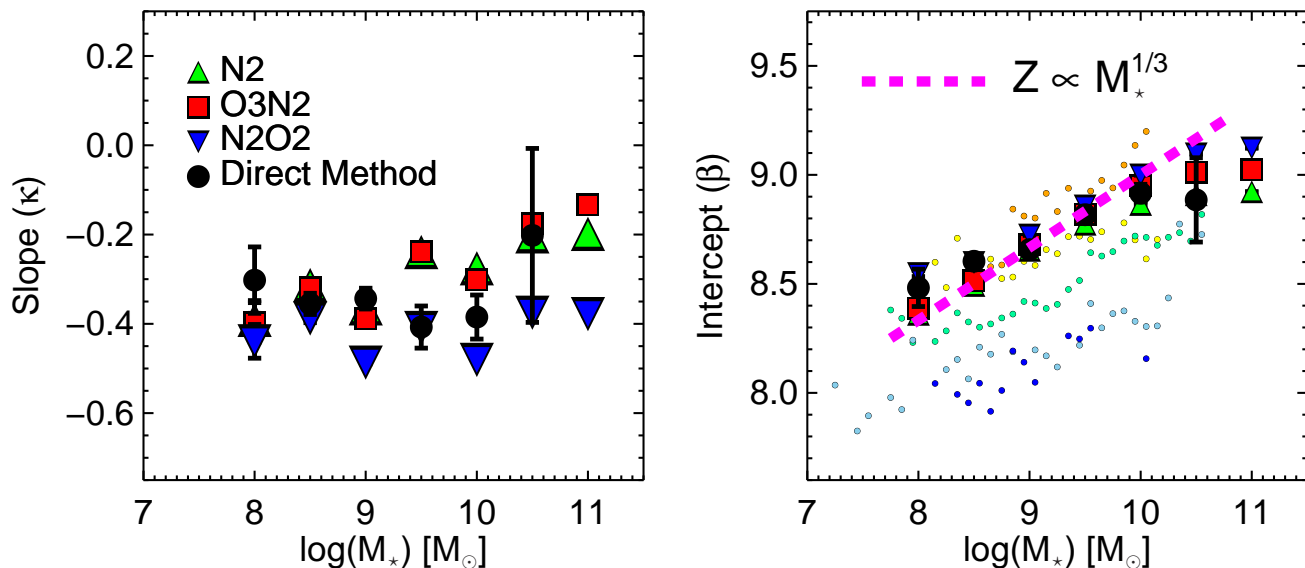


Figure 13. Slopes and intercepts as a function of M_* for our new strong line calibrations (applied to individual galaxies, green, red, and blue points) and direct method measurements (black points). Left: Slope as a function of M_* . The slopes measured from the strong line calibrations typically agree with those measured from the direct method stacks. The instances of disagreement are likely due to the fact that the direct method abundances are more easily measured at high $\Delta \log(\text{SSFR})$, where the relation between $\log(\text{O}/\text{H})$ and $\Delta \log(\text{SSFR})$ appears to steepen. Right: Intercept as a function of M_* . The intercept corresponds to the inferred metallicity of the star forming main sequence. The small circles show where the stacks fall in this parameter space. The stacks are colored according to $\Delta \log(\text{SSFR})$. The measured intercepts closely track the star forming main sequence, which roughly follows the dashed magenta line corresponding to $Z \propto M_*^{1/3}$.

slope of the galaxies (stacks). Interestingly, the N2O2 diagnostic removes much of the nonlinearity of the relationship between $\log(\text{O}/\text{H})$ and $\Delta \log(\text{SSFR})$; the green and red lines agree across a wide range of $\Delta \log(\text{SSFR})$. Furthermore, the slope remains relatively steep, even at high masses, which is not the case for the other diagnostics.

The results of the linear fits for each diagnostic are shown in Figure 13. The left panel shows the measured slope (for both the SDSS galaxies and direct method stack abundances). The right panel shows the corresponding intercept for each fit; the small circles show where the stacks fall in the $M_* - Z$ plane. The measured intercepts (right panel) closely track the star forming main sequence, which also follows the $Z \propto M_*^{1/3}$ scaling denoted by the dashed magenta line. This is consistent with momentum driven winds and a mass loading parameter η which scales approximately as $\eta \propto M_*^{-1/3}$ (Murray et al. 2005; Oppenheimer & Davé 2006).

The left panel of Figure 13 presents clear evidence for evolution of the slope κ as a function of M_* for the N2 and O3N2 diagnostics. The slope is steeper at lower masses, in agreement with previous studies (Ellison et al. 2008; Salim et al. 2014). We measure $\kappa \sim -0.2$ to -0.4 . Andrews & Martini (2013) measured $\alpha = 0.66$ and the slope of the FMR to be 0.43 with the direct method. Converting their direct method α to an equivalent value of κ yields $\kappa \sim -0.28$, which is in good agreement with our measurements. Furthermore, the tension between the slope derived from direct method abundances and that derived from strong line inferred abundances is significantly reduced from that found in Andrews & Martini (2013). Our values of κ are on average steeper than Salim et al. (2014) found. This

is at least in part due to the fact that our new calibrations incorporate $\Delta \log(\text{SSFR})$ explicitly.

The nonlinear dependence of $\log(\text{O}/\text{H})$ on $\Delta \log(\text{SSFR})$ is most prominent in the low mass panels of Figure 11. There is a break in slope between $\log(\text{O}/\text{H})_{\text{N2}}$ and $\Delta \log(\text{SSFR})$, which appears to denote a boundary between highly star forming galaxies and more moderately star forming galaxies. Salim et al. (2014, 2015) interpret this break and the general flattening of the slope with M_* in the context of models from Zahid et al. (2014a). They suggest that the ISM of the more evolved galaxies is saturated and thus the gas phase abundances are largely insensitive to inflows of pristine gas and the resulting variations in $\Delta \log(\text{SSFR})$. In contrast, the more vigorously star forming galaxies have lower gas phase abundances which are more sensitive to inflows of pristine gas. However, the flattening in slope could also be due to the N2 diagnostic losing sensitivity at high metallicities. This would not, however, explain the similar behavior seen for the O3N2 diagnostic (see Figure 13) which is expected to remain sensitive to oxygen abundance in the high metallicity regime.

The break in slope is not present in Figure 12 for N2O2. Furthermore, the slope in Figure 12 is relatively steep and constant for all M_* . Since the N2O2 diagnostic is insensitive to ionization parameter, this may mean that the ionization parameter is more tightly coupled to $\Delta \log(\text{SSFR})$ in intensely star forming galaxies. For instance, suppose an increase in SFR in a highly star forming galaxy produced a larger increase in ionization parameter than in a more moderately star forming galaxy with the same stellar mass. This would bias the N2 and O3N2 diagnostics in the direction of lower metallicity and cause the slope between inferred

$\log(\text{O}/\text{H})$ and $\Delta \log(\text{SSFR})$ to steepen. This would explain why the break is present for N2 and O3N2, but not N2O2. We emphasize that Figures 11 and 12 show how changes in M_* and $\Delta \log(\text{SSFR})$ affect the diagnostics, from which we only *infer* a metallicity. While the break in slope may be a real effect resulting from the physical processes governing the M_* - Z -SFR relation, there remain potential biases associated with strong line calibrations.

5.3 Application of New Calibrations to High Redshift Galaxies

Most galaxies found in high redshift surveys are qualitatively similar to gas rich, metal poor, highly star forming galaxies in the local universe (Steidel et al. 2014; Kriek et al. 2014; Shapley et al. 2015; de los Reyes et al. 2015). This is at least in part a selection effect. At high redshift, bright emission line galaxies are easier to detect than quiescent galaxies. However, the average SFR and SSFR of the universe does indeed increase with redshift, peaking near $z \sim 2$ (e.g., see the compilation by Hopkins & Beacom 2006). In this section we investigate how the mean properties of high redshift galaxies compare to those of local star forming galaxies, as well as whether or not the diagnostic tools developed from galaxies in the local universe can yield useful information when applied to high redshift galaxies.

5.3.1 Are the Calibrations Valid at High Redshift?

The calibrations derived in Section 4 incorporate M_* and $\Delta \log(\text{SSFR})$ relative to the local star forming main sequence. When applying these calibrations to high redshift galaxies there is an implicit comparison to the local star forming main sequence, rather than the star forming main sequence of the high redshift universe. Since the average star formation rate of the universe evolves with redshift, so does the star forming main sequence. In this sense, the local star forming main sequence is a somewhat arbitrary (albeit convenient) zero point for our calibrations. Utilizing a $\Delta \log(\text{SSFR})$ defined relative to the high redshift star forming main sequence would require recalibrating the diagnostics using high redshift galaxies. This would merely amount to a zero-point shift (Salim et al. 2015), since in our framework the higher (S)SFRs would be balanced by lower metallicities.

One possible concern is whether or not it is appropriate to apply our calibrations to high redshift galaxies. Steidel et al. (2014) argue that the position of high redshift galaxies in the BPT diagram is largely independent of (O/H) , and primarily determined by the ionization parameter Γ , which is highly dependent on T_{eff} , the density of star formation, and geometrical effects. They find that the correlation between (O/H) and the strong line ratios is most likely a result of the correlation between Γ , T_{eff} , and the stellar metallicity which, for young stellar populations, reflects the gas phase metallicity. The average T_{eff} may indeed evolve with redshift due to the compact, gas rich, low metallicity environments that become more common at higher redshifts. These conditions could result in stellar populations with abnormally hard ionizing spectra that drive unusual ionization conditions and abundances (Eldridge & Stanway 2009;

Brott et al. 2011; Levesque et al. 2012; Kudritzki & Puls 2000; Kewley et al. 2013). Steidel et al. (2014) show that a factor of 2.5 change in Γ has the same order of magnitude effect on N2 as a factor of five change in Z . Even in the local universe, a factor of 2.5 variation in ionization parameter from one object to another is not unreasonable (Zahid et al. 2012a), although the $z \sim 2.3$ galaxies would require a *systematic* increase in ionization parameter of this order of magnitude. While there is evidence that the ionization conditions of high redshift galaxies are similar to local H II regions (Nakajima et al. 2013), the validity of local strong line calibrations at high redshift is further complicated by the fact that the abundance of nitrogen relative to oxygen may increase with redshift (Steidel et al. 2014; Masters et al. 2014).

While we do not yet have direct method oxygen abundances for a large sample of $z \geq 2$ galaxies, Brown et al. (2014) measured the direct method oxygen abundances and strong line ratios of several Lyman Break Analogs (LBAs; Heckman et al. 2005; Hoopes et al. 2007; Basu-Zych et al. 2007; Overzier et al. 2008, 2009, 2010; Gonçalves et al. 2010). LBAs are local ($z \sim 0.2$) versions of the Lyman Break Galaxies which dominated the SFR of the universe at $z \gtrsim 2.5$ (for a review of LBGs, see Giavalisco 2002). In the left panel of Figure 14 we compare the oxygen abundance determined with our new calibrations with the direct method (O/H) for the four LBAs from Brown et al. (2014). The circles, triangles, and inverted triangles denote the deviation of the inferred (O/H) from the direct method (O/H) for our N2, O3N2, and N2O2 calibrations respectively. The gray shaded region shows the average uncertainty of the direct method measurements.

The choice of star formation rate indicator is a source of systematic error. Our calibrations are derived using the SFRs from the MPA/JHU pipeline. In order to minimize systematic effects associated with the SFR of LBAs, we adopt the SFRs from the MPA/JHU catalog, which agree with the $\text{H}\alpha$ derived SFRs from Overzier et al. (2009). While the $\text{H}\alpha + 24\mu\text{m}$ SFRs from Overzier et al. (2009) are regarded as the optimal SFR indicator, these values are systematically high compared to the $\text{H}\alpha$ derived SFRs and result in correspondingly low oxygen abundances. Thus we recommend $\text{H}\alpha$ derived SFRs when applying these calibrations.

In general, the oxygen abundances predicted by our new calibrations and the direct method oxygen abundances for these LBAs agree quite well. The biggest difference is the N2O2 based metallicity of the most massive LBA from Brown et al. (2014), J005527, which is 1σ larger than the direct method metallicity. However, this object displays features consistent with Wolf-Rayet stars, which may drive unusual (N/O) ratios (Pagel et al. 1986; Henry et al. 2000; Brinchmann et al. 2008; López-Sánchez & Esteban 2010; Berg et al. 2011). We conclude that our new calibrations are suitable for use in LBAs, and that our new calibrations will produce reliable oxygen abundance estimates in the high redshift universe if the ionization conditions of LBAs are representative of their high- z counterparts. Nevertheless, direct method abundance measurements for high redshift galaxies are still needed to determine if local calibrations are suitable for high redshift galaxies.

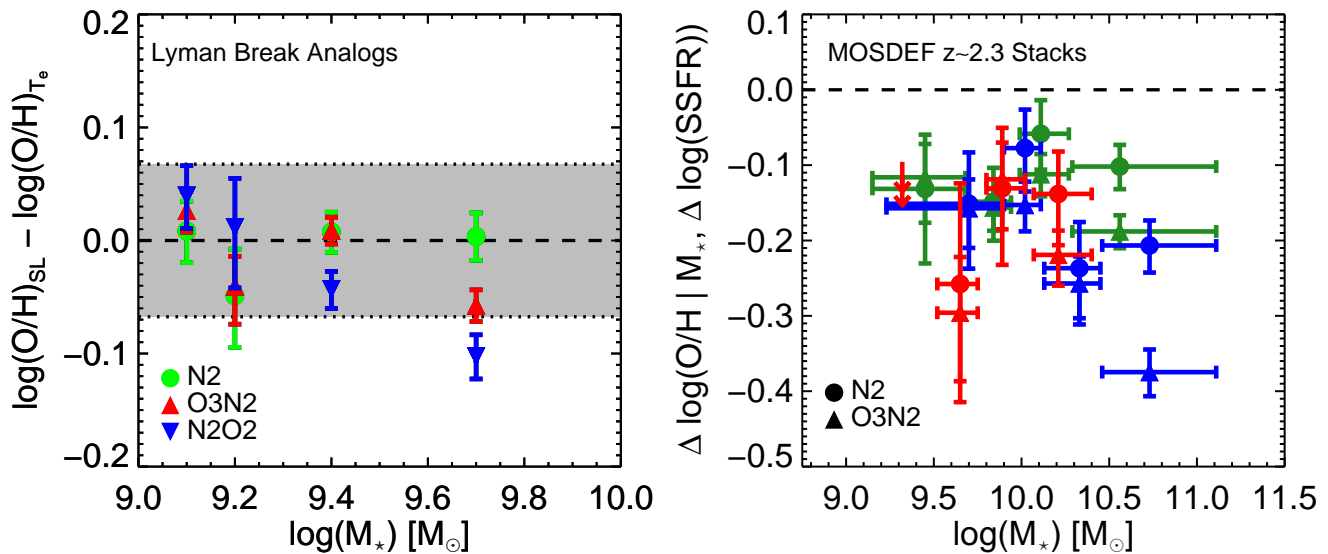


Figure 14. Left: Deviation in strong line (SL) inferred (O/H) from the direct method (O/H) for the 4 LBAs ($z \sim 0.2$) from [Brown et al. \(2014\)](#). The error bars are generated from the Monte Carlo technique previously described (see Section 3.1). The gray band shows the average uncertainty in the direct method oxygen abundances. The oxygen abundances determined with our new strong line calibrations are generally consistent with the measured direct method abundances. Right: Deviation in (O/H) of high redshift galaxies from local galaxies of the same mass and SFR. The MOSDEF $z \sim 2.3$ points are from the [Sanders et al. \(2015\)](#) stacks. The blue, red, and green denote their high, low, and composite SFR stacks respectively. Both our N2 (circles) and O3N2 (triangles) calibrations are shown. The error bars in the mass direction show the range of M_* for each bin and the error bars in Δ (O/H) are generated from the Monte Carlo technique previously described (see Section 3.1). The high redshift galaxies have lower (O/H) than local galaxies of the same M_* and SFR regardless of mass, SFR, or strong line diagnostic.

5.3.2 Application to MOSDEF $z \sim 2.3$ Galaxies

The MOSFIRE Deep Evolution Field (MOSDEF) survey ([Kriek et al. 2014](#)) is a spectroscopic survey investigating the rest frame optical emission lines of high redshift star forming galaxies. [Sanders et al. \(2015\)](#) used a sample of MOSDEF galaxies to stack spectra in M_* and M_* -SFR bins in order to measure the rest frame optical emission lines of $z \sim 2.3$ galaxies with high precision. We use the published M_* , SFR, and emission line data from [Sanders et al. \(2015\)](#) to calculate $\Delta \log(\text{SSFR})$ relative to the local star forming main sequence. We apply our new strong line calibrations to the high and low SFR stacks from [Sanders et al. \(2015\)](#) (shown as crosses in Figures 8 and 9). We determine the uncertainty in oxygen abundances using a Monte Carlo technique similar to that used to determine the uncertainties in our own abundances (see Section 3.1). The error bars in the M_* direction show the mass range of galaxies in the stack. These galaxies fall well below the local MZR. This is in agreement with [Sanders et al. \(2015\)](#), and other studies which have shown that high redshift, highly star forming galaxies tend to have low gas phase oxygen abundances (e.g. [Erb et al. 2006](#); [Maiolino et al. 2008](#); [Maier et al. 2014](#)).

Conceptually, if the gas fueling the star formation has low metallicity, then the ISM of highly star forming galaxies will be relatively metal poor ([Ellison et al. 2008](#); [Mannucci et al. 2010](#); [Lara-López et al. 2010](#)). However, Figures 8 and 9 also show that high redshift galaxies from [Sanders et al. \(2015\)](#) are metal poor relative to our low- z stacks with similar M_* and SFR. The right panel of Figure 14 shows a quantitative comparison of where high redshift galaxies fall relative to local galaxies with similar

M_* and SFR. We find that the high redshift galaxies from [Sanders et al. \(2015\)](#) have metallicities that are on average $\sim 0.1 - 0.2$ dex lower than local galaxies of the same M_* and SFR. There is also evidence that the offset in $\log(\text{O}/\text{H})$ increases with M_* , as noted in [Salim et al. \(2015\)](#). This trend holds for both N2 and O3N2. We did not apply our N2O2 calibration as the $[\text{O} \text{ II}] \lambda 3727 \text{ \AA}$ line does not fall within the spectral range of the MOSFIRE data reported by [Sanders et al. \(2015\)](#). The offset of the [Sanders et al. \(2015\)](#) galaxies toward lower oxygen abundances than local galaxies with the same M_* and SFR appears to contradict the existence of an FMR, and requires some redshift dependence of the M_* - Z -SFR relation.

[Zahid et al. \(2014a\)](#) use analytic and numerical models to quantify the evolution in their datasets. Their model, which they refer to as the Universal Metallicity Relation (UZR), assumes all galaxies evolve along the star forming main sequence. They model the MZR at any epoch as

$$12 + \log(\text{O}/\text{H}) = Z_{\text{O}} + \log \left[1 - \exp \left(- \left[\frac{M_*}{M_{\text{O}}} \right]^{\gamma} \right) \right]. \quad (11)$$

They find that the shape of the MZR is constant (i.e. universal). Only the characteristic turnover mass M_{O} increases with redshift such that at fixed M_* , O/H decreases with redshift. Above M_{O} , galaxies have essentially the same metallicity Z_{O} .

[Salim et al. \(2015\)](#) suggest that the high metallicities act as a buffer against inflows diluting the ISM, resulting in the break in κ seen in the top panels of Figure 11. With a sufficiently large sample of high redshift galaxies resolving the turnover in the MZR, it may be possible to directly

test the evolution of M_O with redshift within the framework of Section 5.2. If M_O increases with redshift as argued by Zahid et al. (2014a), the break in κ should occur at a higher mass than observed for local samples of galaxies. Salim et al. (2015) examine the M_* - Z -SFR relation with the high redshift galaxies from Steidel et al. (2014), as well as local galaxies with relatively high values of $\Delta \log(\text{SSFR})$. Their results suggest that κ flattens at *high* $\Delta \log(\text{SSFR})$, but current samples of high redshift galaxies are not yet complete enough to reveal a break in κ at lower values of $\Delta \log(\text{SSFR})$.

6 SUMMARY

We have recalibrated strong line diagnostics with direct method oxygen abundances of galaxies and applied the new calibrations to investigate the M_* - Z -SFR relation. We stacked $\sim 2 \times 10^5$ spectra of star forming galaxies in the local universe in M_* and offset from the star forming main sequence. Our main results are:

- We recalibrated the relationship between $(\text{O}/\text{H})_{\text{Tc}}$ and the N2, O3N2, N2O2 strong line ratios. This included incorporation of $\Delta \log(\text{SSFR})$ as an additional parameter.
- For the N2 and O3N2 diagnostics we find a higher (O/H) normalization, but similar slope, as previous calibrations. We attribute this difference to the fact that previous calibrations are based on individual H II regions. No single calibration significantly outperforms the others. The O3N2 diagnostic is the most accurate of the three for 43% (47/110) of the stacks, but N2O2 is typically a close second and subject to fewer biases.
- We apply our new calibrations to local star forming galaxies. In the context of galaxy evolution models, our result that the slope of our new calibrations is similar to previous calibrations implies the scaling of galactic outflows with stellar mass remains unchanged.
- We adopt the non-parametric framework presented in Salim et al. (2014) to investigate the M_* - Z -SFR relation in the local universe. When using the N2 and O3N2 diagnostics we find variation in the SFR dependence with both M_* and $\Delta \log(\text{SSFR})$, as noted in previous studies. The N2O2 diagnostic produces a nearly constant slope, independent of M_* and $\Delta \log(\text{SSFR})$. Below $\log(M_*/M_\odot) \sim 10$, the slopes measured with strong line diagnostics are in agreement with each other and consistent with the direct method slope to within $\sim 10\%$. At higher masses, the uncertainty in the direct method slope increases significantly, and the N2 and O3N2 inferred slopes flatten compared to N2O2. We note a modest reduction of scatter in $\log(\text{O}/\text{H})$ at fixed M_* and $\Delta \log(\text{SSFR})$.
- We also apply our new calibrations to high redshift galaxies presented in Sanders et al. (2015). We find these galaxies to be systematically metal poor compared to local galaxies of the same M_* and SFR, and conclude the M_* - Z -SFR relation evolves with redshift.
- It is possible that our O/H estimates of high redshift galaxies are biased by the ionization conditions of the high redshift universe. While direct method measurements of high redshift galaxies are required to definitively test if this is the case, we apply our new calibrations to the LBAs from

Brown et al. (2014) and find consistent results with the direct method measurements of those systems.

There remains some degree of uncertainty as to whether or not these calibrations are valid in the high redshift universe. The ideal path forward would be to recalibrate these empirical relations at $z \sim 2.3$. While direct method oxygen abundance determinations at high redshift are challenging, recent progress has been made. There have been several direct method abundance measurements obtained at $z \sim 1$ (Hoyos et al. 2005; Kakazu et al. 2007; Amorín et al. 2010, 2012), and Yuan & Kewley (2009) used gravitational lensing to measure $[\text{O III}] \lambda 4363$ at $z \sim 1.7$. Most recently, Jones et al. (2015) showed that α element strong line abundance diagnostics are reliable up to at least $z \sim 0.8$. Additionally, Steidel et al. (2014) report that direct method oxygen abundances (in addition the $[\text{O II}]$, $[\text{O III}]$, $\text{H}\alpha$, $\text{H}\beta$, $[\text{N II}]$, and $[\text{S II}]$ optical strong lines) will soon be available for a subset of the KBSS-MOSFIRE targets at $z \approx 2.36 - 2.57$. This will improve constraints on the M_* - Z -SFR relation and ionization conditions in the early universe.

While we have restricted ourselves to two applications of our newly derived calibrations (the M_* - Z -SFR relation and the high redshift universe), there are many other potential applications of these calibrations. For example, a set of abundance diagnostics based on direct method abundances of galaxies rather than individual H II regions is invaluable for any study concerned with gas phase abundances of galaxies, such as transient surveys like ASASSN (Shappee et al. 2014) and ZTF (Bellm 2014). There are also many applications to IFU spectroscopic galaxy surveys (e.g. MaNGA, Bundy et al. 2015), particularly in regions of galaxies where the weak lines are not detected. Lastly, next generation galaxy surveys like DESI (Flaugher & Bebek 2014) will be able to make use of these calibrations to study much larger samples of galaxies.

ACKNOWLEDGEMENTS

We thank Roberto Maiolino, Gwen Rudie, Samir Salim, Ryan Sanders, and Chuck Steidel for comments on an early draft. We also appreciate many helpful comments and suggestions by the referee.

We appreciate the MPA-JHU group for making their catalog publicly available.

The STARLIGHT project is supported by the Brazilian agencies CNPq, CAPES and FAPESP and by the France-Brazil CAPES/Cofecub program.

Funding for the SDSS and SDSS-II has been provided by the Alfred P. Sloan Foundation, the Participating Institutions, the National Science Foundation, the U.S. Department of Energy, the National Aeronautics and Space Administration, the Japanese Monbukagakusho, the Max Planck Society, and the Higher Education Funding Council for England. The SDSS Web Site is <http://www.sdss.org/>.

The SDSS is managed by the Astrophysical Research Consortium for the Participating Institutions. The Participating Institutions are the American Museum of Natural History, Astrophysical Institute Potsdam, University of Basel, University of Cambridge, Case Western Reserve University, University of Chicago, Drexel University, Fermilab, the Institute for Advanced Study, the Japan Participation

Group, Johns Hopkins University, the Joint Institute for Nuclear Astrophysics, the Kavli Institute for Particle Astrophysics and Cosmology, the Korean Scientist Group, the Chinese Academy of Sciences (LAMOST), Los Alamos National Laboratory, the Max-Planck-Institute for Astronomy (MPIA), the Max-Planck-Institute for Astrophysics (MPA), New Mexico State University, Ohio State University, University of Pittsburgh, University of Portsmouth, Princeton University, the United States Naval Observatory, and the University of Washington.

REFERENCES

- Abazajian K. N., et al., 2009, *ApJS*, 182, 543
- Alloin D., Collin-Souffrin S., Joly M., Vigroux L., 1979, *A&A*, 78, 200
- Amorín R. O., Pérez-Montero E., Vílchez J. M., 2010, *ApJ*, 715, L128
- Amorín R., Pérez-Montero E., Vílchez J. M., Papaderos P., 2012, *ApJ*, 749, 185
- Andrews B. H., Martini P., 2013, *ApJ*, 765, 140
- Baldwin J. A., Phillips M. M., Terlevich R., 1981, *PASP*, 93, 5
- Basu-Zych A. R., et al., 2007, *ApJS*, 173, 457
- Belfiore F., et al., 2015, *MNRAS*, 449, 867
- Bellm E., 2014, in Wozniak P. R., Graham M. J., Mahabal A. A., Seaman R., eds, *The Third Hot-wiring the Transient Universe Workshop*. pp 27–33 ([arXiv:1410.8185](https://arxiv.org/abs/1410.8185))
- Berg D. A., Skillman E. D., Marble A. R., 2011, *ApJ*, 738, 2
- Berg D. A., Skillman E. D., Garnett D. R., Croxall K. V., Marble A. R., Smith J. D., Gordon K., Kennicutt Jr. R. C., 2013, *ApJ*, 775, 128
- Berg D. A., Croxall K. V., Skillman E. D., Pogge R. W., Moustakas J., Groh-Johnson M., 2015, preprint ([arXiv:1501.02270](https://arxiv.org/abs/1501.02270))
- Bianco F. B., Modjaz M., Oh S. M., Fierroz D., Liu Y., Kewley L., Graur O., 2015, preprint, ([arXiv:1505.06213](https://arxiv.org/abs/1505.06213))
- Binette L., Wilson A. S., Storchi-Bergmann T., 1996, *A&A*, 312, 365
- Blanc G. A., Kewley L., Vogt F. P. A., Dopita M. A., 2015, *ApJ*, 798, 99
- Bresolin F., Ryan-Weber E., Kennicutt R. C., Goddard Q., 2009a, *ApJ*, 695, 580
- Bresolin F., Gieren W., Kudritzki R.-P., Pietrzyński G., Urbaneja M. A., Carraro G., 2009b, *ApJ*, 700, 309
- Brinchmann J., Charlot S., White S. D. M., Tremonti C., Kauffmann G., Heckman T., Brinkmann J., 2004, *MNRAS*, 351, 1151
- Brinchmann J., Kunth D., Durret F., 2008, *A&A*, 485, 657
- Brott I., et al., 2011, *A&A*, 530, A115
- Brown J. S., Croxall K. V., Pogge R. W., 2014, *ApJ*, 792, 140
- Bundy K., et al., 2015, *ApJ*, 798, 7
- Campbell A., Terlevich R., Melnick J., 1986, *MNRAS*, 223, 811
- Cardelli J. A., Clayton G. C., Mathis J. S., 1989, *ApJ*, 345, 245
- Cenarro A. J., et al., 2007, *MNRAS*, 374, 664
- Charlot S., Longhetti M., 2001, *MNRAS*, 323, 887
- Cid Fernandes R., Mateus A., Sodré L., Stasińska G., Gomes J. M., 2005, *MNRAS*, 358, 363
- Cid Fernandes R., Mateus A., Sodré L., Stasińska G., Gomes J. M., 2011, *STARLIGHT: Spectral Synthesis Code* (ascl:1108.006)
- Considère S., Coziol R., Contini T., Davoust E., 2000, *A&A*, 356, 89
- Davé R., Finlator K., Oppenheimer B. D., 2006, *ArXiv Astrophysics e-prints*
- Davé R., Oppenheimer B. D., Finlator K., 2011a, *MNRAS*, 415, 11
- Davé R., Finlator K., Oppenheimer B. D., 2011b, *MNRAS*, 416, 1354
- De Robertis M. M., Dufour R. J., Hunt R. W., 1987, *J. R. Astron. Soc. Canada*, 81, 195
- Denicoló G., Terlevich R., Terlevich E., 2002, *MNRAS*, 330, 69
- Dinerstein H. L., 1990, in Thronson Jr. H. A., Shull J. M., eds, *Astrophysics and Space Science Library Vol. 161, The Interstellar Medium in Galaxies*. pp 257–285
- Dopita M. A., Evans I. N., 1986, *ApJ*, 307, 431
- Dopita M. A., Kewley L. J., Heisler C. A., Sutherland R. S., 2000, *ApJ*, 542, 224
- Dopita M. A., Sutherland R. S., Nicholls D. C., Kewley L. J., Vogt F. P. A., 2013, *ApJS*, 208, 10
- Edmunds M. G., Pagel B. E. J., 1984, *MNRAS*, 211, 507
- Eldridge J. J., Stanway E. R., 2009, *MNRAS*, 400, 1019
- Ellison S. L., Patton D. R., Simard L., McConnachie A. W., 2008, *ApJ*, 672, L107
- Erb D. K., Shapley A. E., Pettini M., Steidel C. C., Reddy N. A., Adelberger K. L., 2006, *ApJ*, 644, 813
- Falcón-Barroso J., Sánchez-Blázquez P., Vazdekis A., Ricciardelli E., Cardiel N., Cenarro A. J., Gorgas J., Peletier R. F., 2011, *A&A*, 532, A95
- Finlator K., Davé R., 2008, *MNRAS*, 385, 2181
- Flaugher B., Bebek C., 2014, in *Society of Photo-Optical Instrumentation Engineers (SPIE) Conference Series*. p. 0, [doi:10.1117/12.2057105](https://doi.org/10.1117/12.2057105)
- García-Rojas J., Esteban C., 2006, *ArXiv Astrophysics e-prints*
- García-Rojas J., Esteban C., 2007, *ApJ*, 670, 457
- Garnett D. R., 1992, *AJ*, 103, 1330
- Gialvalisco M., 2002, *ARA&A*, 40, 579
- Gonçalves T. S., et al., 2010, *ApJ*, 724, 1373
- Heckman T. M., et al., 2005, *ApJ*, 619, L35
- Henry R. B. C., Edmunds M. G., Köppen J., 2000, *ApJ*, 541, 660
- Hoopes C. G., et al., 2007, *ApJS*, 173, 441
- Hopkins A. M., Beacom J. F., 2006, *ApJ*, 651, 142
- Hoyos C., Koo D. C., Phillips A. C., Willmer C. N. A., Guhathakurta P., 2005, *ApJ*, 635, L21
- Izotov Y. I., Stasińska G., Meynet G., Guseva N. G., Thuan T. X., 2006, *A&A*, 448, 955
- Izotov Y. I., Guseva N. G., Fricke K. J., Henkel C., 2015, *MNRAS*, 451, 2251
- Jones T., Martin C., Cooper M. C., 2015, preprint ([arXiv:1504.02417](https://arxiv.org/abs/1504.02417))
- Kakazu Y., Cowie L. L., Hu E. M., 2007, *ApJ*, 668, 853
- Kashino D., et al., 2013, *ApJ*, 777, L8
- Kauffmann G., et al., 2003a, *MNRAS*, 341, 33
- Kauffmann G., et al., 2003b, *MNRAS*, 346, 1055
- Kennicutt Jr. R. C., Bresolin F., Garnett D. R., 2003, *ApJ*, 591, 801
- Kewley L. J., Dopita M. A., 2002, *ApJS*, 142, 35
- Kewley L. J., Ellison S. L., 2008, *ApJ*, 681, 1183
- Kewley L. J., Jansen R. A., Geller M. J., 2005, *PASP*, 117, 227
- Kewley L. J., Groves B., Kauffmann G., Heckman T., 2006, *MNRAS*, 372, 961
- Kewley L. J., Dopita M. A., Leitherer C., Davé R., Yuan T., Allen M., Groves B., Sutherland R., 2013, *ApJ*, 774, 100
- Kobulnicky H. A., Kewley L. J., 2004, *ApJ*, 617, 240
- Kobulnicky H. A., Kennicutt Jr. R. C., Pizagno J. L., 1999, *ApJ*, 514, 544
- Köppen J., Hensler G., 2005, *A&A*, 434, 531
- Kriek M., et al., 2014, preprint ([arXiv:1412.1835](https://arxiv.org/abs/1412.1835))
- Kriss G., 1994, in *Crabtree D. R., Hanisch R. J., Barnes J., eds, Astronomical Society of the Pacific Conference Series Vol. 61, Astronomical Data Analysis Software and Systems III*. p. 437
- Kudritzki R.-P., Puls J., 2000, *ARA&A*, 38, 613
- Lara-López M. A., et al., 2010, *A&A*, 521, L53
- Lequeux J., Peimbert M., Rayo J. F., Serrano A., Torres-Peimbert S., 1979, *A&A*, 80, 155

- Levesque E. M., Leitherer C., Ekstrom S., Meynet G., Schaerer D., 2012, *ApJ*, 751, 67
- Liang Y. C., Hammer F., Yin S. Y., Flores H., Rodrigues M., Yang Y. B., 2007, *A&A*, 473, 411
- Lilly S. J., Carollo C. M., Pipino A., Renzini A., Peng Y., 2013, *ApJ*, 772, 119
- López-Sánchez Á. R., Esteban C., 2010, *A&A*, 517, A85
- Maier C., Lilly S. J., Ziegler B. L., Contini T., Pérez Montero E., Peng Y., Balestra I., 2014, *ApJ*, 792, 3
- Maiolino R., et al., 2008, *A&A*, 488, 463
- Mannucci F., Cresci G., Maiolino R., Marconi A., Gnerucci A., 2010, *MNRAS*, 408, 2115
- Marino R. A., et al., 2013, *A&A*, 559, A114
- Markwardt C. B., 2009, in Bohlender D. A., Durand D., Dowler P., eds, *Astronomical Society of the Pacific Conference Series* Vol. 411, *Astronomical Data Analysis Software and Systems XVIII*. p. 251 ([arXiv:0902.2850](https://arxiv.org/abs/0902.2850))
- Masters D., et al., 2014, *ApJ*, 785, 153
- McCall M. L., Rybski P. M., Shields G. A., 1985, *ApJS*, 57, 1
- McGaugh S. S., 1991, *ApJ*, 380, 140
- Moustakas J., et al., 2011, preprint ([arXiv:1112.3300](https://arxiv.org/abs/1112.3300))
- Murray N., Quataert E., Thompson T. A., 2005, *ApJ*, 618, 569
- Nakajima K., Ouchi M., Shimasaku K., Hashimoto T., Ono Y., Lee J. C., 2013, *ApJ*, 769, 3
- Nicholls D. C., Dopita M. A., Sutherland R. S., 2012, *ApJ*, 752, 148
- Noeske K. G., et al., 2007, *ApJ*, 660, L43
- Oppenheimer B. D., Davé R., 2006, *MNRAS*, 373, 1265
- Overzier R. A., et al., 2008, *ApJ*, 677, 37
- Overzier R. A., et al., 2009, *ApJ*, 706, 203
- Overzier R. A., Heckman T. M., Schiminovich D., Basu-Zych A., Gonçalves T., Martin D. C., Rich R. M., 2010, *ApJ*, 710, 979
- Pagel B. E. J., Edmunds M. G., Blackwell D. E., Chun M. S., Smith G., 1979, *MNRAS*, 189, 95
- Pagel B. E. J., Terlevich R. J., Melnick J., 1986, *PASP*, 98, 1005
- Pagel B. E. J., Simonson E. A., Terlevich R. J., Edmunds M. G., 1992, *MNRAS*, 255, 325
- Peimbert M., 1967, *ApJ*, 150, 825
- Pettini M., Pagel B. E. J., 2004, *MNRAS*, 348, L59
- Pilyugin L. S., 2003, *A&A*, 399, 1003
- Pilyugin L. S., Thuan T. X., 2005, *ApJ*, 631, 231
- Pilyugin L. S., Mattsson L., Vílchez J. M., Cedrés B., 2009, *MNRAS*, 398, 485
- Pilyugin L. S., Vílchez J. M., Thuan T. X., 2010, *ApJ*, 720, 1738
- Pilyugin L. S., Grebel E. K., Mattsson L., 2012, *MNRAS*, 424, 2316
- Salim S., et al., 2007, *ApJS*, 173, 267
- Salim S., Lee J. C., Ly C., Brinchmann J., Davé R., Dickinson M., Salzer J. J., Charlot S., 2014, *ApJ*, 797, 126
- Salim S., Lee J. C., Davé R., Dickinson M., 2015, preprint ([arXiv:1506.03080](https://arxiv.org/abs/1506.03080))
- Sánchez-Blázquez P., et al., 2006, *MNRAS*, 371, 703
- Sánchez S. F., et al., 2012, *A&A*, 538, A8
- Sánchez S. F., et al., 2013, *A&A*, 554, A58
- Sánchez S. F., et al., 2014, *A&A*, 563, A49
- Sanders R. L., et al., 2015, *ApJ*, 799, 138
- Schlegel D. J., Finkbeiner D. P., Davis M., 1998, *ApJ*, 500, 525
- Searle L., 1971, *ApJ*, 168, 327
- Shapley A. E., Coil A. L., Ma C.-P., Bundy K., 2005, *ApJ*, 635, 1006
- Shapley A. E., et al., 2015, *ApJ*, 801, 88
- Shappee B. J., et al., 2014, *ApJ*, 788, 48
- Shaw R. A., Dufour R. J., 1995, *PASP*, 107, 896
- Skillman E. D., et al., 2013, *AJ*, 146, 3
- Stasińska G., 1982, *A&AS*, 48, 299
- Stasińska G., 2006, *A&A*, 454, L127
- Steidel C. C., et al., 2014, *ApJ*, 795, 165
- Storchi-Bergmann T., Calzetti D., Kinney A. L., 1994, *ApJ*, 429, 572
- Stoughton C., et al., 2002, *AJ*, 123, 485
- Tremonti C. A., et al., 2004, *ApJ*, 613, 898
- Vazdekis A., Sánchez-Blázquez P., Falcón-Barroso J., Cenarro A. J., Beasley M. A., Cardiel N., Gorgas J., Peletier R. F., 2010, *MNRAS*, 404, 1639
- Vila Costas M. B., Edmunds M. G., 1993, *MNRAS*, 265, 199
- Whitaker K. E., van Dokkum P. G., Brammer G., Franx M., 2012, *ApJ*, 754, L29
- Yates R. M., Kauffmann G., Guo Q., 2012, *MNRAS*, 422, 215
- Yuan T.-T., Kewley L. J., 2009, *ApJ*, 699, L161
- Zahid H. J., Bresolin F., Kewley L. J., Coil A. L., Davé R., 2012a, *ApJ*, 750, 120
- Zahid H. J., Dima G. I., Kewley L. J., Erb D. K., Davé R., 2012b, *ApJ*, 757, 54
- Zahid J., Dima G., Kudritzki R., Kewley L., Geller M., Hwang H. S., 2014a, preprint ([arXiv:1404.7526](https://arxiv.org/abs/1404.7526))
- Zahid H. J., et al., 2014b, *ApJ*, 792, 75
- Zaritsky D., Kennicutt Jr. R. C., Huchra J. P., 1994, *ApJ*, 420, 87
- de los Reyes M. A., et al., 2015, *AJ*, 149, 79

This paper has been typeset from a $\text{\TeX}/\text{\LaTeX}$ file prepared by the author.